ABSTRACT

The effects of cementite particles and subgrain boundaries on work-hardening behavior of spheroidized carbon steels were investigated by making direct measurements of residual internal stresses. These internal stresses developed due to plastic incompatabilities between elastic particles and an elastic-plastic matrix. A continuum analysis of these internal stress fields, based upon a multiple slip model, is presented and is found to be in good accord with the experiments. The internal stresses appear to saturate in the plastic strain range of 3 ~ 5% where a transition in strain-hardening behavior was observed ("double-n" behavior), and to contribute approximately 20% to total work-hardening. The cementite-particle-pinned-subgrain-boundaries, formed during a post-quench annealing treatment, were found to lower the internal stress, thus indicating that they assisted the relaxation processes of entrapped Orowan loops by acting as sources of dislocations. The flow stress increment in dispersion hardened alloys due to work-hardening consisted of internal stress, forest stress, and source-shortening stress. The flow stress curves of spheroidized carbon steels were found to be described by a modified mean-square-root addition law of the form

$$\sigma_f = \sigma_{\varepsilon_p=0} + \sigma^i + \left[(\Delta\sigma^s)^2 + (\Delta\sigma^{ss})^2 + (\sigma^f)^2 \right]^{1/2} .$$

The maximum normal interfacial stresses were estimated from the data. The maximum values occurred in the tensile direction at the poles of particles and the magnitude was found to be approximately one half of flow stress. The significance of these stresses regarding interface cavitation is discussed briefly.

Page

TABLE OF CONTENTS

1. INTRODUCTION

When work hardenable metals are cyclically deformed by forward and then reversed loading, they typically exhibit a decrement in the magnitude of the reversed yield stress [1]. The effect, which is found in a wide class of pure metals and alloys, including both single crystals and polycrystals, is generally believed to be a consequence of the internal stresses that develop due to the inhomogeneity of plastic deformation [2].

In polycrystalline alloys that contain large second phase inclusions, especially inclusions that do not undergo any appreciable plastic deformation, a large part of the overall strain-hardening results from directional long-range stresses. These stresses are the same kind that give rise to the aforementioned Bauschinger effects and are caused by an incompatibility of plastic strain between the particles and the surrounding plastic matrix [3]. In recent years, continuum and dislocation models for this sort of anisotropic hardening [4,5,6,7] have been developed (these models are reviewed and developed in later sections) and they have been successfully applied to particle hardened alloys. The models always predict enhanced Bauschinger effects and a particularly interesting manifestation of directional internal stresses that we call, following Wilson [8], permanent softening. Permanent softening is illustrated graphically in Figure 3.1 and because it plays a central role in the present work, it is explained in detail in Section 3.1.

Now since the models we will use relate both the overall work-hardening behavior and the Bauschinger effects to the details of the residual dislocation structure left at the particle-matrix interfaces, it appears to be possible to extract information from direct measurements of these effects concerning, for example, the local stresses and elastic strains developed within the inclusions and at the particle-matrix interfaces during plastic deformation. Such information would in turn be very helpful in explaining, 1) the observed changes in work-hardening behavior, which is found to occur at certain strain levels [9,10], 2) the influence of particle size and particle volume fraction on work hardening, and 3) the process of particle cavitation (i.e. separation of the particle-matrix interface) which is known to be promoted by large values of the interfacial stresses. The research program reported here is in fact concerned with the use of these models and the relevant experimental data to explain the micro-mechanics of work-hardening and internal stress development in dispersion hardened steels.

With the above objectives in mind, a series of experiments was conducted on two plain carbon steels, heat treated to contain spheroidal carbides in the 0.6~2μm diameter size range. All the relevant strain-hardening parameters for simple tensile straining, as well as the reversed deformation characteristics for tension-compression cycling, were measured. The magnitudes of the Bauschinger effect and the permanent softening were also measured and were correlated with such microstructural parameters as particle size and volume fraction.

In the quenched and tempered state, it is found that the carbides are generally interlinked with a network of dislocation subgrain boundaries. To determine the influence of these subgrain boundaries on the work-hardening behavior and internal stress levels, additional tests were conducted on alloys specifically heat treated to remove the subgrain boundaries while maintaining the particle sizes within the range common to the alloys containing subgrains. As was mentioned earlier, the directional long-range stresses which tend to "harden" the matrix are caused by the dense clustering of dislocations at the particle-matrix interfaces. These clusters cause large stresses within the particles which are counter-balanced in an average way by stresses in the matrix. It will be explained later that the permanent softening is a measure of these stresses and can be used to estimate the local stresses acting on the particles. In Section 5.1, an analysis of the interfacial stresses for spherical inclusions is presented.

In Sections 2 and 3 a brief but relevant review is given of the various modellistic approaches to boundary and particle hardening. In particular a thorough discussion is provided in Section 3 for particle strengthening and internal stresses; permanent softening is explained and its relation to observed Bauschinger effects, and to the local stresses acting at the particles, is made clear. The experimental techniques that were used and the results obtained are presented in Section 4. Finally, the results are discussed in Section 5.

2. BOUNDARY STRENGTHENING

2.1 Grain Boundary Strengthening

It is well known that the presence of grain boundaries in all polycrystalline materials provides strength by interfering with the motion of dislocations. A very useful relation between the yield stress and the grain size, viz. the Hall-Petch equation, is now well established for low carbon steels [11,12];

$$\sigma_y = \sigma_0 + k_y d^{-1/2} \quad . \tag{2.1}$$

In Equation (2.1), σ_y is the yield stress, d is the average grain size, and σ_0 and k_y are constants. Equations (2.1) has been confirmed experimentally for many materials other than steels [13,14,15] and has been derived theoretically from dislocation pile up models [12, 16] and dislocation interaction work-hardening models [17,18].

In the pile up models, the grain boundaries are assumed to be strong barriers to the glide dislocations, and thus the dislocations are queued at, or "piled up" against, them. These pile ups intensify the net force on the lead dislocation in analogy with the stress concentrations at the tips of shear cracks. Yielding occurs when this stress concentration at the leading dislocation, τ_{tip}, exceeds a critical stress, τ_{crit}. For an isolated single ended dislocation pile up of n dislocations for example, τ_{tip} is, as virtual work implies,

$$\tau_{tip} = n\left(\tau^A - \tau_0\right) \quad . \tag{2.2}$$

In Equation (2.2), τ_0 is a frictional stress which fluctuates on the spatial scale of the lattice parameter and τ^A is the applied shear stress. n, in turn, is expressable in terms of the slip line length, ℓ (an experimentally measurable quantity), as

$$n = \left(\tau^{A} - \tau_{0}\right) \ell / 2A \;, \tag{2.3}$$

where A has the value of $\mu b/2\pi$ and $\mu b/2\pi(1-\nu)$ for screw and edge dislocations, respectively (μ = shear modulus, b = Burgers vector, and ν = Poisson's ratio).

Equation (2.3) is derived by assuming a continuous distribution of dislocations, although discrete dislocation models yield similar results [19]. Taking ℓ equal to d and equating τ_{tip} to τ_{crit}, we obtain the above form of the Hall-Petch relation:

$$\tau_y = \tau_0 + \left(2A\,\tau_{crit}\right)^{1/2} d^{-1/2} \;. \tag{2.4}$$

The analyses leading to Equation (2.1) can be extended to describe the flow stress as long as the grain boundaries continue to act as barriers to moving dislocations [20]; in this case the flow stress, σ_f, is given by

$$\sigma_f = \sigma_{0f} + k_f d^{-1/2} \;, \tag{2.5}$$

where the parameter k_f now depends on the plastic strain.

The lack of direct evidence of pile ups at the grain boundaries in many cases has motivated the development of strain-hardening models in which the grain size is related to the dislocation density produced during deformation. For example, Nabarro et al. [21] have reviewed a variety of proposed flow stress and dislocation density, ρ, relationships and have shown that the relation

$$\tau_f = \tau_{0f} + c\mu b \rho^{1/2} \;, \tag{2.6}$$

where c is a constant whose value in the various model versions ranges from 1/3 to 1/5, is a general form which is derived from a wide class of work-hardening theories. Ashby [22] on the other hand in one particular study related the dislocation density to the structural parameters λ^G and λ^S defined by him as the "geometric slip" distance and "statistical slip" distance, respectively. He assumed that the total dislocation density was composed of both the dislocations which are "geometrically necessary" to accomodate the plastic non-homogeneities across the grain boundaries and the "statistically stored dislocations" which would accumulate in a matrix without particles as they do, say, in single crystals. Taking ρ^G and ρ^S as the densities of these two types of dislocations, Ashby writes for the total density:

$$\rho^T = \rho^G + \rho^S . \tag{2.7}$$

Simple additivity in Equation (2.7), we note, is doubtful since it ignores the interactions between grain boundary processes and grain matrix slip. Thompson et al. [23] have suggested instead that each such term should be corrected by the respective area fractions so that the polycrystal is viewed as a kind of composite structure with a hard boundary region and a softer grain matrix. In the case where $\rho^G >> \rho^S$, however, it is always assumed that $\rho^T \cong \rho^G$ and ρ^G is related geometrically to λ^G as

$$\rho^G = 4\gamma_p / b\lambda^G , \tag{2.8}$$

where γ_p is the shear strain.

Ashby [22] has further assumed that λ^G, instead of the more commonly used dislocation slip distance [24,25], is proportional to the grain size. The average Taylor orientation factors, $\langle M \rangle$, whose values are calculated as 3.067 for f.c.c. polycrystals [26] and as 2.733 for b.c.c. polycrystals deforming by pencil glide [27], relate the shear stress, τ, and strain, γ, to the tensile stress, σ, and strain, ε, as [26]

$$\langle M \rangle = \sigma / \tau = d\gamma_p / d\varepsilon_p \,. \tag{2.9}$$

Substituting Equation (2.8) into (2.6) and converting to tensile stress and tensile strain by utilizing a Taylor factor, we obtain again a Hall-Petch type equation,

$$\sigma_f = \sigma_{0f} + c' \mu \langle M \rangle^{3/2} \left(b \varepsilon_p \right)^{1/2} d^{-1/2} \,, \tag{2.10}$$

which in addition predicts a parabolic stress-strain relation.

Ashby [22] has also used Equation (2.10) to interpret results on strain-hardening for dispersion strengthened single crystals [28,29] by noting that λ^G is given by r/f for equiaxed inclusions, where r and f are the particle radius and the particle volume fraction, respectively.

Thus, the particle hardening effect, $\Delta\sigma^P$, is

$$\Delta\sigma^P = c' \langle M \rangle^{3/2} \mu \left(b f \varepsilon_p / 2r \right)^{1/2} . \tag{2.11}$$

In Equation (2.10) and (2.11), c' is a constant having the value (0.25 ± 0.15). Although the Ashby model has had some success in describing the work-hardening behavior of dispersion hardened crystals, this model does not account for the detailed dislocation arrangements and so makes no predictions concerning the Bauschinger effect.

On the other hand, we note that all these theoretical approaches seem invariably to lead to a flow stress (and yield stress) which varies as the relevant microstructural distance, i.e. grain size, raised to the inverse square root power. The flow stress is then found to vary parabolically with plastic strain. These two features are amenable to experimental verification.

2.2 Dislocation Substructure Strengthening

The mechanism of cell formation is now believed to be the formation of dislocation tangles, which gradually join into three dimensional networks[30,31]. Subgrain boundaries, on the other hand, are generally observed to form under conditions where significant dynamic or static recovery occurs either during or after plastic deformation [32]. Holt [33] has analyzed a model for cell formation which assumes that the driving force for dislocation cell formation is a reduction in the total elastic energy of dislocations due to their clustering in cell walls. The model has a clear analogy to the process of spinodal decomposition [34]. He has shown that spatial fluctuations in an initially uniform density of dislocations with certain periodicities can grow faster than others and that the wave lengths of the fastest growing density perturbations are proportional to the inverse of the square root of the uniformly distributed dislocation density, ρ,

$$L^{-1} = K \rho^{1/2} . \tag{2.12}$$

In Equation (2.12), K is a constant and L is the average cell size. Substituting Equation (2.12) into (2.6), it is found that

$$\sigma_f = \sigma_{0f}^{(S)} + K_f^{(S)} L^{-1} , \tag{2.13}$$

where $k_f^{(s)}$ is another constant defined as cμb/K. Equation (2.13) should hold under conditions of steady state deformation such as are attained in hot working where the average dislocation density remains essentially constant[35,36].

Young and Sherby[74] have also shown that subgrain boundary strengthening behavior in a number of iron based alloys can be described by Equation (2.13). They have further asserted that subgrains can indeed play a dominant role in the strengthening, especially in the range of subgrain sizes that are less than about 0.4μm.

However, it has also been reported that much of the data for yield stress can be fitted to a Hall-Petch type equation [30],

$$\sigma_y^{(S)} = \sigma_0^{(S)} + k_y^{(S)} L^{-1/2} , \tag{2.14}$$

thus implying that the subgrains may have a similar effect on strain-hardening behavior as do the grain boundaries. Theoretical approaches have been made to rationalize Equation (2.14) by analyzing the stress fields of simple tilt sub-boundaries based upon either the pile up [21,37] or forest hardening[38] models. The absence of direct observation of dislocation pile ups at sub-boundaries favors the forest models which are concerned with the stresses to force dislocations through the dislocation debris formed as a result of unpinning of boundary dislocations [30]. Li [17] has derived a Hall-Petch type equation using such a forest model which has the form

$$\tau_y = \tau_0^{(s)} + \left[\mu b/2\pi(1-\nu)\right] \left[8\theta/\pi b\right]^{1/2} L^{-1/2} . \tag{2.15}$$

The analysis predicts that the yield stresses depends on both the subgrain size and the average misorientation of subgrain, θ.

A majority of the experimental data, however, shows that the yield strength is independent of the misorientation angle of subgrain boundaries and only depends on their size via Equation (2.15) [30]. An interesting point to be noted is that well-recovered materials tend to obey the relation of

Equation (2.13). That is, the observations [39] suggest that the exponents of subgrain size change from values near -1 to values closer to -1/2 as recovery proceeds.

Another noteworthy feature of sub-boundaries is the fact that they produce vanishing long-range stresses as has been suggested by Kuhlmann-Wilsdorf [40,41]. She has constructed a "building block" model of the terminated loop hexapoles composed of edge and screw dislocations, in which a conditional minimum energy criterion has been imposed and has suggested that the tilt and twist cell walls in adjacent cells most likely consist of equal and opposite dislocation densities. From the results of simulated stress fields, she has reported that there exist two kinds of long-range stresses: (1) long-range multipolar stress fields which attract dislocations to the cell wall and eventually vanish and (2) rotational stress fields arising from the rotational stresses of a single hexapole which have also been shown to be cancelled by constructing a multi-hexapolar model in an alternating sense of rotation [42]. A variety of transmission electron microscopic observation of dislocation substructure [43] supports the assumption of a reduced long-range stress field along the sub-boundaries. A continuum analysis for the elastic fields of periodic dislocation networks [44] has also shown that the rotational fields in a periodic planar distribution of dislocation networks decrease exponentially with distance and vanish on the average. There do exist observations, however, that indicate that cell walls in the deformed structure do produce some long-range elastic stress fields [43].

Thus it is not clear from existing knowledge exactly how the sub-boundaries contribute to strain-hardening behavior. Bearing this in mind, we attempt here to understand the role of subgrain boundaries in spheroidized carbon steels on the hardening behavior from the internal stress measurements discussed in Section 5.4.

3. PARTICLE STRENGTHENING

Orowan [45] has proposed a dislocation bypass model for dispersion strengthened materials and has given the critical shear stress, τ_c, to bow a glide dislocation as

$$\tau_c = 2T/b\Lambda \tag{3.1}$$

Where T is the idealized dislocation "line tension" and Λ is the interparticle distance. In recent years, a number of theoretical approaches have been proposed to analyze the strain-hardening behavior of dispersion hardened materials which in fact are based on the original Orowan model [46]. For the purpose of discussion we will classify them as; (1) forest type hardening models [47,48] which emphasize the interaction between glide dislocations and the "forest" dislocations produced by certain dislocation relaxation mechanisms and (2) back stress hardening models [3,4,6,7,8], which deal with the internal stresses due to the Orowan loops. Furthermore, we note that the role of these internal stresses in strain-hardening has been treated from two rather different points of view. One approach deals with the back stress of a long-range character [3,4,6,7,8], whereas the other is primarily concerned with the local fluctuating stress around each particle [49,50]. The various dispersion hardening theories based on internal stress concepts are reviewed and compared briefly in this section.

3.1 FHP Model [49] and Revised Hart Model [50]

The Fisher, Hart, and Pry (FHP) model is based on the assumption that the strain-hardening process in the matrix proceed as they would in, for example, a single crystal matrix without particles. They have further assumed that plastic flow occurs in a single slip fashion and thus, the glide dislocations are piled up against particles. We note that this is a somewhat unrealistic assumption, especially in the light of recent work on deformation process at large inclusions [51,52]--a point we consider in more detail later on. In the FHP model, the maximum hardening increment, τ_h^{max}, due to the, elastically deforming, particles over the pure matrix flow stress was estimated. At large strains they obtained for τ_h^{max},

$$\tau_h^{max} = 1.3\beta K\left[N_c b/r_s\right]\mu f^{3/2}, \quad (3.2)$$

where β is a constant taken to be equal to 3. N_c is the maximum number of shear loops a particle can maintain, K is defined as $[1 + \nu/2(1-\nu)]$ and r_s is the mean square planar radius which is related to the mean particle radius statistically as

$$r^2 = 3r_s^2/2 . \quad (3.3)$$

Since the number of shear loops is related to the shear strain as

$$\gamma_p = Nb/2r , \quad (3.4)$$

Equation (3.2) can be rewritten in the form

$$\tau_h^{max} = 12\mu\gamma_p^* f^{3/2}, \quad (3.5)$$

where γ_p^* is a critical shear strain at which the number of shear loops becomes saturated and the numerical constant 12 is obtained by setting $\nu = 1/3$. τ_h^{max} is in fact identified as the <u>saturation</u> back stress and thus Equation (3.5) predicts that the back stress hardening depends on particle volume fraction raised to the 3/2 power. Ashby has obtained the same result from a so-called "elastic peg" model [53]. The FHP model, however, does not account for the Orowan stress and so it estimates only the maximum hardening increment due to the presence of particles.

Hart [50] has recently modified the FHP model to account for the Orowan stress and has obtained a stress-strain relation which assumes (1) that the Orowan stress is simply additive to the matrix flow stress and (2) that the back stress effect caused by the local fluctuating stresses of the Orowan loops acts so as to raise the critical stress for subsequent dislocation bowing. From the fundamental assumption of simple linearly additive flow stress contributions, the hardening increment due to particles is defined as

$$\tau_h = \tau_{MP} - \tau_M \,, \qquad (3.6)$$

where τ_{MP} and τ_M represent the flow stresses of the specimens containing particles and without particles, respectively. Hart [50] has further modelled the trapped shear loops as being infinitestimal in size and has taken for their stress field the field of a shear dislocation dipole. The critical shear stress required to force a glide dislocation between two trapped loop dipoles was calculated and can be expressed as

$$\tau_h = \tau_0 \left[1 + 2M^{1/2} + 2M\right] , \qquad (3.7)$$

where $M = 0.509\ K(\mu/\tau_0)\gamma_p^u\ f^{3/2}$ (γ_p^u: unrelaxed plastic shear strain). This shear stress-shear strain relation was then converted to a tensile stress-strain relation using simple Taylor averaging, $\langle M \rangle$, to obtain

$$\sigma_h = \sigma_0 + 1.6 \langle M \rangle \left(\mu/\sigma_0\right)^{1/2} f^{3/4} \left(\varepsilon_p^u\right)^{1/2} + 1.28 \langle M \rangle^2 \mu f^{3/2} \varepsilon_p^u \,, \qquad (3.8)$$

where ε_p^u is the unrelaxed tensile plastic strain and σ_0 is the tensile equivalent of the Orowan stress.

Asaro[4] has refined the computation of the Orowan stress by considering the effect of more complicated distributions of shear loops. The results are consistent with those of Equation (3.7) and can be represented in the slightly more general form as

$$\tau_h = \tau_0\left[1 + \omega\left(M + M^{1/2}\right)\right] , \qquad (3.9)$$

where ω is a constant ranging from 0.5 to 2.0 and M is a linear function of strain. The experimentally measured value of the hardening increment in general includes an additional stress--the image stress, τ^{im},--which is a long-range residual stress associated with the finite size of the body[4,7]. This reversible residual stress has been shown to be a dominant contribution to the strain-hardening at large strains--this effect is discussed in the next section.

3.2 Wilson's Construction and the Bauschinger Effect

It has already been noted that both continuum and microscopic models predict the existence of long-range internal stresses and the accompanying pronounced Bauschinger effects caused by plastic incompatibilities between non-deforming inclusions and elastic-plastic matrices. Asaro[4] has suggested at least three kinds of kinematic-type hardening behavior which might result when the macroscopic internal stresses are related to the details of microstructures. These macroscopic residual internal stresses developed during unidirectional deformation can be removed by reverse straining. This kind of behavior leads to the permanent softening effect[2] we discussed earlier. The magnitude of this permanent softening simply appears as the difference in flow stress for reversed and forward deformation evaluated at some large strain, as illustrated in Figure 3.1. Wilson [8] has shown that internal stresses are linearly related to the magnitude of the permanent softening, σ^{PS}, by correlating measurements of the Bauschinger effect to the average internal stress, σ^{i}, measured by monitering X-ray diffraction line shifts. His experimental results show that the residual internal stress is about one half of the magnitude of permanent softening. Although he concluded that σ^{i} and σ^{PS} are the lower and the upper limits of the back stress hardening element, Asaro [4] and Brown [54] took the internal stress to be equal to one half the measured permanent softening--this assumption is based upon a "shake down" model for dispersion hardened materials [55]. To appreciate this point of view, we consider the simple elastic-plastic element model of Figure 3.2. The elastic regions (viz. strong elements, inclusions, or boundaries) support stresses which are transmitted as residual stresses to the plastic region (viz. weak elements or matrices) upon unloading. Thus, the model shows a Bauschinger effect, manifested by a permanent softening whose magnitude, as can be seen from the figure, is just twice the residual internal stress. The inhomogeneous local stresses around the particles are believed to produce the characteristically rounded part of the reverse stress-strain curve [54]. This argument has been confirmed by Brown et al. [54] by defining a parameter β empirically as

$$|\sigma_r|/\sigma_f = \beta\, \varepsilon_r^{1/2}. \qquad (3.10)$$

β was found to be proportional to the inverse of the measured value of permanent softening. Moan et al. [56] have also obtained the same result by describing the forward flow stress and the backward flow stress as

$$\sigma_f = \sigma_0 + \sigma^i + \sigma^f$$

and

$$\sigma_r = \sigma_0 - \sigma^i + \sigma^f , \qquad (3.11)$$

where σ^f stands for the "forest stress". Thus, σ^i can be expressed in the form

$$\sigma^i = \left[\sigma_f - |\sigma_r|\right]/2 = \sigma^{PS}/2 \ . \qquad (3.12)$$

It should be further noted that the internal stress is in fact a measure of the Bauschinger energy parameter, β_E, which has been proposed as a measure of the Bauschinger effect [57]. β_E has been defined as

$$\beta_E = E_S/E_T = \langle\sigma_E\rangle/\langle\sigma_T\rangle \ ; \qquad (3.13)$$

E_S and E_T are the elastic energy stored in forward deformation and the total energy required to give forward deformation, respectively, and $\langle\sigma_T\rangle$ is the average forward tensile stress. The average stress, $\langle\sigma_E\rangle$, which is related to elastic energy stored by $E_S = \langle\sigma_E\rangle \epsilon_T$, is believed by the author to be just another expression for the residual internal stress. Asaro [4] has further indicated that regardless of the details of the initial reverse flow, the difference between the forward and reverse flow stress curves asymtotically approaches the value $2\sigma^i$ for all three kinematic-type hardening cases. Since these models, however, do not depend on the fine details of the microstructures, as does the "source-shortening" or "Orowan stress" contributions, they give the sort of overall average internal stresses which are measured in the present work.

3.3 Tanaka and Mori Model

Instead of directly computing the forces acting on the glide dislocations, Tanaka and Mori [6] have computed the isothermal free energy change of an elastic-plastic specimen containing elastic particles. If the elastic constants of the matrix and particles are the same*, the free energy change during the deformation by a uniaxial tensile stress, σ_{33}^{A}, is

$$\Delta G = N\left(E_{el}+E_{int}\right)+\sigma_0\varepsilon_p V_M-\left(\sigma_{33}^{A}\right)^2 V/2E-\sigma_{33}^{A}\varepsilon_p V\,, \qquad (3.14)$$

where N is the number of inclusions, σ_0 is the yield stress of the matrix (identified as the Orowan stress), V_M and V are the volume of the matrix and the specimen, respectively, and ε_p is the imposed uniform plastic strain in the matrix. The elastic energy, E_{el}, and the interaction energy, E_{int}, are calculated according to the well known scheme devised by Eshelby [58].

The specimen is assumed to undergo a dilatation free extension corresponding to a plastic strain, ε_p, in x_3 direction. Since the particles do not deform plastically, Orowan shear loops are left around inclusions as a result of the bypassing of dislocations. These loops give rise to plastic incompatibility between the elastic-plastic matrix and the elastic inclusions. The central assumptions in this model are that these loops are distributed uniformly at the particle-matrix interface and that the plastic deformation in the matrix occurs by uniform symmetrical multiple slip. This assumption

---

*Although accurate values of the elastic constants of cementite are not available, it is believed that the elastic constants of polycrystalline cementite have rather similar values to those of ferrite [52].

enabled these authors to make use of Eshelby's "uniform transformation strain" results [58] by identifying the transformation strain components, ε_{ij}^{T}, with the plastic strains as follows,

$$\varepsilon_{11}^{T} = \varepsilon_{22}^{T} = \varepsilon_{p}^{u}/2 \ , \ \ \varepsilon_{33}^{T} = -\varepsilon_{p}^{u} \ , \tag{3.15}$$

and $\varepsilon_{ij}^{T} = 0$ otherwise.

The model is depicted in Figure 3.3(a) and (b). The dislocation loop distributions envisioned in the FHP and revised Hart models are also illustrated in Figure 3.3(c) for the sake of comparison. For spherical inclusions, the stresses inside the inclusion and the constrained strains, ε_{ij}^{C}, are given as

$$\sigma_{ij}^{I} = 2\mu\left(\varepsilon_{ij}^{C} - \varepsilon_{ij}^{T}\right)$$

and (3.16)

$$\varepsilon_{ij}^{C} = \left[2\left(4-5\nu\right)/15\left(1-\nu\right)\right]\varepsilon_{ij}^{T} \ .$$

From Equations (3.15) and (3.16), we obtain the following stress components inside the inclusion:

$$\sigma_{33}^{I} = 2\mu\alpha\,\varepsilon_{p}^{u}$$

and (3.17)

$$\sigma_{11}^{I} = \sigma_{22}^{I} = -\mu\alpha\,\varepsilon_{p}^{u} \ ,$$

where α is the accomodation factor, which for the case of a sphere, is equal to (7-5ν)/15(1-ν). The elastic energy stored during the deformation and the interaction energy of the internal stress field due to the applied stress are

$$E_{el} = -\frac{1}{2}\int_{V_I} \sigma_{ij}^{I}\,\varepsilon_{ij}^{I}\,dV = 3V_I\mu\alpha\left(\varepsilon_{p}^{u}\right)^2/2 \tag{3.18}$$

and
$$E_{int} = -\int_{V_I} \sigma_{ij}^{A}\, \varepsilon_{ij}^{T}\, dV = \sigma_{33}^{A} V_I\, \varepsilon_P^{u} , \tag{3.19}$$

where V_I is the volume of the inclusions.

Substituting Equations (3.18) and (3.19) into Equation (3.14) and using the stability conditions, $\partial(\Delta G)/\partial(\varepsilon_p^{u}) = 0$ and $\partial^2(\Delta G)/\partial^2(\varepsilon_p^{u}) > 0$, the following stress-strain relation was obtained

$$\sigma_{33}^{A} = \sigma_0 + 3\mu\alpha\left(f/1-f\right)\varepsilon_p^{u} . \tag{3.20}$$

The procedure predicts a linear hardening behavior which depends on particle volume fraction only and not on any other feature of the particle distribution. The flow stress calculated in this manner certainly represents a lower bound to the true value, since it is assumed that all the work done by the applied stress is stored as elastic energy (that is, dissipation is ignored). The equivalence of this model to that of FHP has been discussed recently [59] and it has been shown that the linear hardening behavior is not necessarily due to the assumption of uniform plastic deformation. This continuum model, however, does not adequately take into account the stress required to bow dislocations around the particles, so that it fails to include a proper treatment of matrix hardening behavior.

3.4 Brown and Stobbs Model

Brown and Stobbs [60] have attempted to describe the macroscopic properties of their own dispersion hardened materials in terms of observed dislocation microstructures. Their model is considered by the present author to be the most realistic and complete of those proposed so far. They have computed the contributions to the flow stress arising from both the forest and the back stress hardening by assuming these effects to be linearly additive. The entrapped Orowan loops plastically relax by various mechanisms such as local climb, cross slip of screw segments to produce prismatic dislocation loops [48], or by secondary slip processes as proposed by Ashby [47]. A secondary plastic zone with a high forest dislocation density is thus produced around the particles, the precise form of which depends on the particular relaxation mechanism. This plastic zone directly hardens the matrix by a forest type hardening and also prohibits subsequent full plastic relaxation of Orowan shear loops, thus stabilizing the localized elastic stress field which is the source of the back stress hardening.

3.4.1 Elastic Model

In the absence of plastic relaxation, back stress hardening is seen as to arise from the internal stresses and the stresses required to bow dislocation between particles [7]. Following Asaro [3], we can estimate these internal stresses by considering a structure whose surfaces are traction free. For this structure we may write

$$\int_V \tau_{ij}\, dV = 0 , \qquad (3.21)$$

thus satisfying the equilibrium condition. Dividing the integration limits into the volume of the matrix and that of the particles, we arrive at the result

$$\langle \tau_{ij}^{M} \rangle + \left(f/1-f \right) \langle \tau_{ij}^{I} \rangle = 0 . \qquad (3.22)$$

Now the traction free boundary conditions give

$$\langle \tau_{ij}^{I} \rangle = \langle \tau_{ij}^{\infty,I} \rangle + \langle \tau_{ij}^{im,I} \rangle . \qquad (3.23)$$

In Equations (3.22) and (3.23), the angular brackets represent the average values, $\tau_{ij}^{\infty,I}$ are the particle stresses computed as if the medium were infinite in extent and $\tau_{ij}^{im,I}$ are the so-called "image stresses" of the particles or actually the corrections to this "infinite" field due to the traction free surfaces. Since $\langle\tau_{ij}^{im,I}\rangle$ is itself proportional to particle volume fraction for ellipsoidal inclusions [61], $\langle\tau_{ij}^{M}\rangle$ can be written, to first order in f, as

$$\langle\tau_{ij}^{M}\rangle = -(f/1-f)\ \langle\tau_{ij}^{\infty,I}\rangle\ . \tag{3.24}$$

$\langle\tau_{ij}^{M}\rangle$ acts as an opposing stress to glide dislocations. The uniform shear stress in a typical inclusion is found to be

$$\langle\tau^{\infty,I}\rangle = \alpha\mu\gamma_p^u \tag{3.25}$$

for the uniform shear model assumed [7]--this is illustrated in Figure 3.3(d). Equations (3.24) and (3.25), when combined with a Taylor factor, $\langle M\rangle$, used again to convert the predicted shear stress-strain relation to a uniaxial tensile stress-strain relation give the stress just after yielding as

$$\sigma^A = \sigma_0 + \langle M\rangle^2 \alpha (f/1-f) \mu \varepsilon_p^u \tag{3.26}$$

In the case of multiple slip, the accomodation factor (α') has been estimated as $\alpha' = \frac{3}{4}\alpha$ for spherical inclusions [6]. If we replace α with $3\alpha/4$ and take $\langle M\rangle$ to be have the value 2[**], then Equation (3.26) is identical to that of

---

[**] Tanaka and Mori's continuum model essentially assumes that plastic flow occurs on numerous slip systems simultaneously; this gives $\langle M\rangle = 2$ [10].

Tanaka and Mori [6]--Equation (3.20). As plastic deformation proceeds, the shortening of effective interparticle distance due to residual Orowan loops raises the bowing stress according to Equation (3.1) and thus the flow stress in this stage of hardening is given, again assuming linear additivity [57] as

$$\sigma^{A} = \sigma_{0}\left[1+(2/\Lambda)\left\{(2\langle M\rangle r^{3}\varepsilon_{p}^{u}/b)^{1/2}-r\right\}\right]+\langle M\rangle^{2}\alpha(f/1-f)\mu\varepsilon_{p}^{u} \; . \qquad (3.27)$$

The "source-shortening" stress in Equation (3.27) has been calculated approximately by assuming a simple constant line tension of $\mu b^2/4$. The stress-strain relation is in fact similar to that computed by Asaro [4] and Hart [50]. One of the major results of this continuum analysis is that the mean local stresses around a particle vanish, contrary to that of Hart and that the local fluctuating stresses give rise to the "source-shortening" stress. A further discussion on the similarities and differences of the Hart, Tanaka and Mori and Brown and Stobbs models has recently been given in references[59,61].

3.4.2 Plastic Relaxation

Plastic relaxation, in general, occurs at the onset of plastic flow, so that any theory which does not properly consider plastic relaxation cannot describe dispersion hardening behavior adequately. Brown and Stobbs [60] have computed a forest hardening term and the back stress hardening term by noting that plastic relaxation occurs in their alloys by secondary slip. They assumed that this "secondary plastic zone" would be plate-like with a radius R and of thickness r--this assumption being suggested by their observations. From Equation (2.6), the local flow stress in the plastic zone can be written in the form

$$\tau_{\mathrm{local}} = c\mu b\rho_{\mathrm{local}}^{1/2} \; . \qquad (3.28)$$

If all the dipoles of prismatic loops which have been converted from Orowan loops are contained in the zone, then the secondary dislocation density in the zone, ρ_{local}, is

$$\rho_{local} = h\,n\,r/V_p \quad , \tag{3.29}$$

where h is a constant taken to be approximately equal to 8. The plastic zone volume, V_p, for their assumed model is

$$V_p = \pi R^2 r \quad , \tag{3.30}$$

in which the particle volume is also included. We will instead explicitly note that the particle volume should be subtracted from V_p, since the particle size is typically of a comparable magnitude to the dimensions of this relaxation zone. The number of relaxed Orowan loops, n, is related to the relaxed plastic shear strain statistically as

$$n = 2r(\gamma_p - \gamma_p^u)/b \ . \tag{3.31}$$

When the particle-matrix interfacial stress, which is found to be $\mu\alpha\gamma_p^u$ for the uniform shear model, exceeds the local flow stress, secondary slip is presumed to occur. This condition, along with Equations (3.28), (3.29), and (3.31), gives the unrelaxed plastic shear strain as

$$\gamma_p^u = [cb/\alpha]\left[2h(\gamma_p - \gamma_p^u)r^2/bV_p\right]^{1/2} \quad , \tag{3.32}$$

where all the parameters are the same as defined previously. Equating the particle stress at the outer edge of the plastic zone to the Frank-Read type stress acting on loop dipoles yields the following relation

$$\mu\alpha\gamma_p^u r^3/R^3 = \mu b/r \ . \tag{3.33}$$

Taking $\gamma_p >> \gamma_p{}^u$ and ignoring the particle volume contained in the plastic zone, the plastic zone radius, R, and the unrelaxed tensile strain, corrected by the Taylor averaging factor, are determined from Equations (3.30), (3.32), and (3.33) to be

$$R=\left[\langle M\rangle 2hc^2 r\varepsilon_p/b\pi\right]^{1/8} r \tag{3.34}$$

and

$$\varepsilon_p{}^u=\left[1.3c^{3/4}/\langle M\rangle^{5/8}\alpha\right]\left[b\pi/hr\varepsilon_p\right]^{1/8}\left[hb\varepsilon_p/\pi r\right]^{1/2}. \tag{3.35}$$

The fraction of bowing dislocations lying in the zone is approximately the square root of the plastic zone volume fraction, f_p, which can be expressed as

$$f_p = 3V_p f/4\pi r^3. \tag{3.36}$$

The "forest stress" caused by the "forest" of secondary dislocations is, by writing $\tau^f = f_p{}^{1/2}\tau_{local}$ and correcting with Taylor averaging, thus given by

$$\sigma^f=\langle M\rangle^{3/2}c\mu\left[3h/\pi\right]^{1/2}\left[bf\varepsilon_p/2r\right]^{1/2} \tag{3.37}$$

This is identical to the result of Ashby [22]--Equation (2.11). Similary, the residual internal stresses are obtained by substituting Equation (3.35) into (3.26) as

$$\sigma^i=1.3\langle M\rangle^{11/8}c^{3/4}\mu\left[f/1-f\right]\left[b\pi/h\varepsilon_p r\right]^{1/8}\left[hb\varepsilon_p/\pi r\right]^{1/2}. \tag{3.38}$$

Equation (3.38) predicts that the back stress hardening depends on (1) the particle volume fraction almost linearly, (2) the plastic strain nearly parabollically and (3) the particle radius raised to the -5/8 power. The above predictions are compared with the results of the present work and are discussed further in Section 5.2.

4. EXPERIMENTAL PROCEDURES AND THE RESULTS

4.1 Heat Treatment and Microstructures

Two steels with different carbon contents, which are listed in Table 4.1, were heat treated to prepare tensile specimens, each steel being prepared with two contrasting microstructures. Steel A was austenitized at 810°C for 2 hours while in the form of round bars with a 5/8" diameter, whereas specimens of steel B were first machined into slightly oversized tensile specimens and then austenitized at 1020°C for 2 hours. Austenitizing, in all cases, was followed by quenching in a 25% aqua oil-water solution. The pre-machining treatment for steel B was used in order to achieve a more homogeneous martensitic transformation throughout the specimen cross section after quenching. The alloys which were tempered isothermally after quenching contained a dispersion of spherical carbides that were interlinked with dislocation subgrain boundaries. The microstructures with these subgrain networks connecting cementite particles were produced by annealing at 700°C for 1 hour, 8 hours, and 40 hours for steel A and for 3 hours for steel B, and are designated as specimen numbers, AT1, AT2, AT3, and BT, respectively. Subgrain free microstructures, with particles inside the grain boundaries, were produced by thermal cycling for 1 hour between 710° ± 5°C and 735° ± 5°C with hold times at each temperature of approximately 3 minutes, and are hereafter designated as specimens with the identifying prefix AC. Thermal cycling was carried out using two lead baths, each maintained at a fixed temperature following the procedures described by Anand [10]. Conventional optical micrographs and standard two stage carbon replica photomicrographs were taken using an optical microscope ("Bauch and Lomb") and an electron microscope ("JEM 30").

The subgrain boundary free microstructures are shown in Figure 4.1 and typical examples of subgrain boundary connected spheroidized cementite microstructures are shown in Figure 4.2 and Figure 4.3.

Quantitative metallographical methods [10,62] were used to determine the following microstructural parameters assuming that a uniform distribution of spherical cementite particles was present:

(1) mean particle radius defined as,

$$r = 3f/4N_p \; ; \qquad (4.1)$$

(2) mean free path of cementite particles,

$$\lambda_p = (1-f)/N_p \; ; \qquad (4.2)$$

(3) mean intercept length of grain boundaries,

$$d = 1/N_G \; ; \qquad (4.3)$$

(4) mean intercept length of subgrain boundaries,

$$L = 1/N_L \; ; \qquad (4.4)$$

(5) mean free path of both particles and subgrains,

$$\lambda_{\ell,p} = (1-f)/N_L \; ; \qquad (4.5)$$

(6) mean-square-lattice spacing,

$$\lambda_{sq} = r_s\left[(\pi/f)^{1/2} - 2\right] \qquad (4.6)$$

where $r_s = (2/3)^{1/2}\, r$. (4.7)

The measured values N_P, N_G, and N_L, are the number of intercepts per unit length of random test lines with the cementite particles, the grain boundaries, and the subgrain boundaries, respectively. These values are listed in Table 4.2 for further reference.

4.2 Testing Apparatus and Procedures

The difficulties involved in obtaining cyclic stress-strain curves are well known and thus a special self-aligning "Woods Metal" grip of composition; Bi-50, Pb-25, Sn-12.5, Cd-12.5; was constructed to facilitate lateral alignment in our push-pull cyclic tests. The tensile specimens had a 1/2" gauge length and a 1/4" diameter gauge section. Threaded grips were used to prevent slipping upon reverse loading. In some of the low strain amplitude tests, 1" gauge length specimens were also used. The specimens used for low amplitude strain cycling were recovered at 400°C for 20 minutes and reused in further cyclic tests.

All the tests were carried out on an MTS closed loop testing machine under strain control using a sinusoidal wave form as the control function. The average extension rate in all the tests was 0.005 inch per minute. The cyclic load-strain curves in each strain range were plotted on an X-Y recorder. An additional forward tensile load-strain curve for each kind of specimens was also obtained to complete the Wilson construction. All the load-strain curves were later converted to true stress-true strain curves for analysis.

4.3 Stress-Strain Data Analysis and Results

Among the several empirical stress-strain relations, the so-called Hollomon equation is most commonly used to explain strain-hardening behavior. The basic form (i.e. power laws) were first proposed by Ludwick and later confirmed by Hollomon[66], among others, as

$$\sigma = k\,\varepsilon^{n} \qquad (4.8)$$

or

$$\sigma = k' \varepsilon_p^{n'} , \qquad (4.9)$$

where k, n, k', and n' are material constants and σ, ε, and ε_p represent the true stress, the true strain, and the true plastic strain, respectively. True stresses and true strains have been computed from the load-elongation curves and the true plastic strains have also been estimated as deviations from linear elastic behavior

$$\varepsilon_p = \varepsilon - \sigma/E , \qquad (4.10)$$

where E is Young's modulus ($E \cong 30 \times 10^6$ psi for iron).

The true stress-true plastic strain curves have been used to measure the amounts of permanent softening at each given pre-strain through the use of Wilson constructions [8] as illustrated in Figure 4.4 for specimens AC. The measured values of Bauschinger effect at given plastic strains are also plotted as a function of reverse plastic strain, ε_r, in Figure 4.5 and it shows that the differences between the forward and the reverse flow stresses asymtotically approach the values of permanent softening. The corresponding internal stresses were taken to be equal to one half the magnitude of the permanent softening.

The log-log plots for both the σ-ε curves and the σ-ε_p curves show a "double-n" type strain-hardening behavior with the transition in the index n occuring at a strain level of 3 ~ 5% true strain. The constants of the Hollomon type equations were determined by the least square analysis method for each range of strains. The calculated values of the constants, designated as k_1, n_1, k_2, and n_2 for Equation (4.8) and k'_1, n'_1, k'_2, and n'_2 for Equation (4.9) are listed in Table 4.3.

Since plastic flow begins in the pre-macro-yield region [10], the stresses at the beginning of plastic flow ($\sigma_{\varepsilon_p = 0}$) were obtained by extrapolating the initial portion of the homogeneous part of the stress-strain curves back to zero plastic strain. At the intersection point of the elastic line and the extrapolated curve, the flow stress for the unstrained specimens are determined using the relation

$$\sigma_{\varepsilon_p = 0} = \left[k_1 / E^{n_1}\right]^{1/1-n} \qquad (4.11)$$

The calculated values of $\sigma_{\varepsilon_p = 0}$ are also listed in Table 4.3.

5. DISCUSSION

5.1 Elastic Stress Field of a Particle

The stress fields enhanced in and around a particle during plastic deformation, which are caused by plastic incompatibilities between the elastic particle and the plastic matrix are now believed to give rise to a back stress hardening. This sort of internal stress has recently been computed from a uniform shear model [7]. The plastic flow, however, in a number of dispersion strengthened materials has in fact been observed to occur on several slip systems simultaneously [51]--especially in spheroidized carbon steels [10]. Thus, we estimate the internal stress fields, formed during uniform plastic flow by symmetrical multiple slip, by making use of Eshelby's transformation results [58].

Let the specimen undergo a uniaxial tensile deformation with imposed plastic strain, ε_p^u, along the x_3 axis; then the transformation strains (Figure 3.3) are

$$\varepsilon_{33}^T = -\varepsilon_p^u , \quad \varepsilon_{11}^T = \varepsilon_{22}^T = \varepsilon_p^u/2$$

and (5.1)

$$\varepsilon_{ij}^T = 0 \qquad \text{otherwise.}$$

The constrained displacement field, u_i^c, in a dilatation free deformation is now calculated as

$$u_i^c = [1/8\pi(1-\nu)]\,\varepsilon_{jk}^T\,\psi_{,ijk} + [1/2\pi]\,\varepsilon_{ik}^T\,\phi_{,k} \qquad (5.2)$$

with the already known harmonic, ϕ, and biharmonic, ψ, potentials for a spherical inclusion:

$$\phi = -\frac{2\pi}{3} R^2 , \qquad \psi = -\frac{\pi}{15} R^4 , \qquad \text{for} \quad R \leqslant r$$

and (5.3)

$$\phi = \frac{4\pi r^3}{3} \frac{1}{R} , \quad \psi = \frac{4\pi r^3}{3} \left(R + \frac{r}{5R} \right), \quad \text{for} \quad R \geqslant r ,$$

where $R^2 = x_1^2 + x_2^2 + x_3^2$.

Equations (5.1), (5.2), and (5.3) yield the following displacement fields: in the matrix,

$$u_1^M = \frac{\varepsilon_p^u}{4(1-\nu)} \frac{r^3}{R^3} x_1 \left\{ \frac{(5-4\nu)}{3} - \frac{3}{5} \frac{r^2}{R^2} - 3\frac{x_3^2}{R^2} + 3\frac{x_3^2 r^2}{R^4} \right\} ,$$

$$u_2^M = \frac{\varepsilon_p^u}{4(1-\nu)} \frac{r^3}{R^3} x_2 \left\{ \frac{(5-4\nu)}{3} - \frac{3}{5} \frac{r^2}{R^2} - 3\frac{x_3^2}{R^2} + 3\frac{x_3^2 r^2}{R^4} \right\} , \qquad (5.4)$$

$$u_3^M = \frac{\varepsilon_p^u}{4(1-\nu)} \frac{r^3}{R^3} x_3 \left\{ \frac{(8\nu-1)}{3} - \frac{9}{5} \frac{r^2}{R^2} - 3\frac{x_3^2}{R^2} + 3\frac{x_3^2 r^2}{R^4} \right\} ,$$

and inside the particles,

$$u_1^I = -(1/2)\ \alpha\ x_1 \varepsilon_p^u ,$$

$$u_2^I = -(1/2)\ \alpha\ x_2 \varepsilon_p^u , \qquad (5.5)$$

$$u_3^I = \alpha\ x_3 \varepsilon_p^u ,$$

where $\alpha = \frac{7 - 5\nu}{15(1-\nu)}$.

The corresponding stress fields in an isotropic medium computed from

$$\sigma_{ij} = \lambda u_{k,k} \delta_{ij} + \mu (u_{i,j} + u_{j,i}) , \qquad (5.6)$$

are:

in the matrix,

$$\sigma_{11}^{M} = \frac{\mu \varepsilon_p^u}{2(1-\nu)} \left[\frac{r^3}{R^3} \left\{ \frac{5(1-2\nu)}{3} + \frac{3(6\nu-4\nu^2-1)}{(1-2\nu)} n_3^2 + (4\nu-5) n_1^2 + 15 n_1^2 n_3^2 \right\} + \frac{r^5}{R^5} \left\{ -\frac{3}{5} + \frac{3(1-4\nu)}{(1-2\nu)} n_3^2 + 3 n_1^2 - 21 n_1^2 n_3^2 \right\} \right],$$

$$\sigma_{22}^{M} = \frac{\mu \varepsilon_p^u}{2(1-\nu)} \left[\frac{r^3}{R^3} \left\{ \frac{5(1-2\nu)}{3} + \frac{3(6\nu-4\nu^2-1)}{(1-2\nu)} n_3^2 + (4\nu-5) n_2^2 + 15 n_2^2 n_3^2 \right\} + \frac{r^5}{R^5} \left\{ -\frac{3}{5} + \frac{3(1-4\nu)}{(1-2\nu)} n_3^2 + 3 n_2^2 - 21 n_2^2 n_3^2 \right\} \right], \tag{5.7}$$

$$\sigma_{33}^{M} = \frac{\mu \varepsilon_p^u}{2(1-\nu)} \left[\frac{r^3}{R^3} \left\{ \frac{(2\nu-1)}{3} + \frac{4(5\nu+\nu^2-2)}{(1-2\nu)} n_3^2 + 15 n_3^4 \right\} + \frac{r^5}{R^5} \left\{ -\frac{9}{5} + \frac{6(3-7\nu)}{(1-2\nu)} n_3^2 - 21 n_3^4 \right\} \right],$$

$$\sigma_{12}^{M} = \frac{\mu \varepsilon_p^u}{2(1-\nu)} \left[\frac{r^3}{R^3} \left\{ (4\nu-5) n_1 n_2 + 15 n_1 n_2 n_3^2 \right\} + \frac{r^5}{R^5} \left\{ 3 n_1 n_2 - 21 n_1 n_2 n_3^2 \right\} \right],$$

$$\sigma_{13}^{M} = \frac{\mu \varepsilon_p^u}{2(1-\nu)} \left[\frac{r^3}{R^3} \left\{ -(2\nu+5) n_1 n_3 + 15 n_1 n_3^3 \right\} + \frac{r^5}{R^5} \left\{ 9 n_1 n_3 - 21 n_1 n_3^3 \right\} \right],$$

$$\sigma_{23}^{M} = \frac{\mu \varepsilon_p^u}{2(1-\nu)} \left[\frac{r^3}{R^3} \left\{ -(2\nu+5) n_2 n_3 + 15 n_2 n_3^3 \right\} + \frac{r^5}{R^5} \left\{ 9 n_2 n_3 - 21 n_2 n_3^3 \right\} \right],$$

and inside the particles,

$$\sigma_{11}^{I} = \sigma_{22}^{I} = -\alpha \mu \varepsilon_p^u ,$$

$$\sigma_{33}^{I} = 2 \alpha \mu \varepsilon_p^u , \tag{5.8}$$

$\sigma_{ij}^{I} = 0$ otherwise.

λ and μ are the Lamé constants and n_i represents the i^{th} component of the unit normal vector on the sphere of radius R. The summation convention is used throughout and a comma implies differentiation with respect to the corresponding spatial coordinate, i.e. $u_{i,j}$ means $\frac{\partial u_i}{\partial x_j}$. The interfacial stress components can be obtained from Equation (5.7) by setting R = r as

$$\begin{aligned}
\sigma_{11}(r) &= \frac{\mu \varepsilon_p^u}{(1-\nu)} \left\{ \frac{(8-25\nu)}{15} + (2\nu-1) n_1^2 + 3\nu n_3^2 - 3 n_1^2 n_3^2 \right\} , \\
\sigma_{22}(r) &= \frac{\mu \varepsilon_p^u}{(1-\nu)} \left\{ \frac{(8-25\nu)}{15} + (2\nu-1) n_2^2 + 3\nu n_3^2 - 3 n_2^2 n_3^2 \right\} , \\
\sigma_{33}(r) &= \frac{\mu \varepsilon_p^u}{(1-\nu)} \left\{ \frac{(5\nu-16)}{15} + (5-\nu) n_3^2 - 3 n_3^4 \right\} , \\
\sigma_{12}(r) &= \frac{\mu \varepsilon_p^u}{(1-\nu)} \left\{ (2\nu-1) n_1 n_2 - 3 n_1 n_2 n_3^2 \right\} , \\
\sigma_{13}(r) &= \frac{\mu \varepsilon_p^u}{(1-\nu)} \left\{ (2-\nu) n_1 n_3 - 3 n_1 n_3^3 \right\} , \\
\sigma_{23}(r) &= \frac{\mu \varepsilon_p^u}{(1-\nu)} \left\{ (2-\nu) n_2 n_3 - 3 n_2 n_3^3 \right\} .
\end{aligned} \tag{5.9}$$

The normal stress, σ_{nn}, shear stress, τ_{ns}, and hydrostatic stress, σ_h, at the particle-matrix interface in the plane of $n_2 = 0$ are now written in the simple form

$$\begin{aligned}
\sigma_{nn}(r) &= \alpha \mu \varepsilon_p^u (3 n_3^2 - 1) , \\
\tau_{ns}(r) &= \alpha \mu \varepsilon_p^u \, 3 n_3 (1 - n_3^2)^{1/2} , \\
\sigma_h (r) &= \mu \varepsilon_p^u \{(1+\nu)/3(1-\nu)\} (3 n_3^2 - 1) .
\end{aligned} \tag{5.10}$$

These stresses are plotted in Figure 5.1. The maximum shear stress is shown to be $\frac{3}{2}\alpha\mu\varepsilon_p^{\ u}$ at $n_3 = 1/\sqrt{2}$ and the maximum normal stress is $2\mu\alpha\varepsilon_p^{\ u}$ at $n_3 = 1$. The stresses inside an inclusion can also be computed more easily from Equation (3.14) and the results are, as expected, found to be identical to those of Equation (3.17). One interesting result of the present computation is that the mean values of σ_{11}^M, σ_{22}^M, and σ_{33}^M do not vanish as they do in the uniform shear model. Since the mean value of $(n_i)^2$ is 1/3 and $(n_i)^2(n_j)^2$ have mean values of 1/15 and 1/5 for $i \neq j$ and $i = j$ respectively, the mean stresses are

$$\langle\sigma_{11}^M\rangle = \langle\sigma_{22}^M\rangle = \langle\sigma_{33}^M\rangle = \mu\,\varepsilon_p^u \frac{\nu}{(1-\nu)(1-2\nu)} \frac{r^3}{R^3}\left(1-\frac{r^2}{R^2}\right) \tag{5.11}$$

and $\langle\sigma_{ij}^M\rangle = 0$ otherwise.

These mean stresses are plotted in Figure 5.2 as a function of R. Although the mean stresses fall off rapidly as $1/R^3$, there are, as shown, relatively high stresses near the particle with a maximum value of $\sim 0.3\mu\varepsilon_p^{\ u}$ (for $\nu = 1/3$) at $R = \sim 1.3r$. We then feel that these kind of fluctuating stresses should be considered in the analysis of the back stress hardening.

5.2 Back Stress Hardening

A number of theories for dispersion hardening have recently been proposed and almost all of them predict the existence of back stress hardening as discussed earlier in Section 3. Among them, the model of Brown and Stobbs is considered to be the most accurate. These models, however, have been concerned with particles of radii less than 3000 Å, so that the particle volume itself has been ignored in the process of computing plastic zone volume--Equation (3.30). This cannot be justified in the present case of large particles. Furthermore, since the plate-like plastic zone shape is a consequence of the uniform shear assumption, for our axi-symmetric deformation we feel that the plastic zone shape in spheroidized carbon steels should be approximately annular around the particles. This assumption is in fact supported by observations of uniform secondary dislocation distributions around such particles [10]. Thus, the plastic zone volume, accounting for these facts, should have the form

$$V_p = (4/3)\,\pi\,(R^3 - r^3)\;. \tag{5.12}$$

The critical stress to start secondary slip is the maximum shear stress at the particle-matrix interface. From Equation (5.10) we obtain the maximum shear stress as

$$\tau_{ns}^{max} = (3/2)\,\mu\,\alpha\,\varepsilon_p^u\;. \tag{5.13}$$

The local flow stress in the plastic zone can now be written in the form

$$\tau_{local} = c\mu b\,\{3hr^2\gamma_p/2\pi b(R^3 - r^3)\}^{1/2}\;. \tag{5.14}$$

Finally, the Frank-Read type stress criterion is

$$(3/4)\,\alpha\mu\gamma_p^u\,(r^3/R^3) = \mu b/r\;. \tag{5.15}$$

Equations (5.13), (5.14), and (5.15) yield a cubic equation for ε_p^u

$$(\langle M\rangle/2)(3\alpha/2)\,r^2(\varepsilon_p^u)^3 - br(\varepsilon_p^u)^2 - (2/\langle M\rangle)(2cb/3\alpha)^2(3h\varepsilon_p/\pi) = 0\,. \tag{5.16}$$

To obtain the relation between ε_p^u and r, Equation (5.16) was solved numerically at various ε_p taking $\langle M \rangle = 2$. The results are plotted in Figure 5.3 for the case of $\varepsilon_p = 0.03$, $\varepsilon_p = 0.04$, and $\varepsilon_p = 0.05$. The least square analysis gives the relation between the particle radius and the unrelaxed plastic strain as

$$\varepsilon_p^u = K_1(\varepsilon_p)\, r^{-0.7}, \qquad (5.17)$$

where $K_1(\varepsilon_p)$ is a constant at the given plastic strain, ε_p. Substituting Equation (5.15) into (3.20) yields for the back stress,

$$\sigma^i = 3\mu\alpha(f/1-f)\; K_1(\varepsilon_p)\, r^{-0.7}. \qquad (5.18)$$

When the measured internal stresses are plotted against the particle radius (Figure 5.4), it is seen that the internal stress depends inversely on the particle radius. Since the particle size dependence of the internal stress is directly related to the plastic relaxation mechanism and thus to the plastic zone shape, it is difficult to predict the particle size dependence more accurately than is done using Equation (5.18) without further details on the dislocation distribution. However, we note that the overall predicted values of internal stresses are in good accord with the measurements for particle radii in the range exceeding 0.5μm. We therefore feel that Equation (5.18) can be applied more generally as long as the particle size is large enough to give a uniform distribution of secondary dislocations.

To obtain the relation between the internal stress and the plastic strain, Equation (5.16) was again solved numerically for each experimental value of r. The results, plotted in Figure 5.5, again show a power relation of the form

$$\varepsilon_p^u = K_2(r)\ \varepsilon_p^{m} \quad , \tag{5.19}$$

where $K_2(r)$ is now a constant at given particle radius and m is approximately obtained as 0.3 for all three particle radii used. The measurements, however, give the value of m as about 0.6 for the tempered specimens (Figure 5.6), which is in fact a factor of two higher than the predicted one. The failure in predicting the plastic strain dependence on internal stress is felt to be due to the reasons already discussed for the particle size dependence. If we substitute Equation (5.19) into (3.20), we can represent the internal stress in the form

$$\sigma^i = 3\mu\alpha(f/1-f)\ K_2(r)\ \varepsilon_p^{0.3} \quad . \tag{5.20}$$

The values of σ^i computed from Equation (5.20) are plotted in Figure 5.7 together with the measured values. We again note that the predicted values are nearly coincident with the measured values in the range ε_p = 0.01 ~ 0.05. The form of Equation (5.19) has been reported by Kishi and Tanabe [63]. They have observed in their experiments that the permanent softening can be expressed in the form

$$\sigma^{PS} = k\ \varepsilon_p^{m} \quad . \tag{5.21}$$

This is identical with Equation (5.19) if we note that σ^{PS} is linearly related to ε_p^u. m has been defined as a Bauschinger effect parameter and Kishi and Tanabe's data [63] show good agreement with the present work.

Now the secondary plastic zone size, η, can be obtained by substituting Equation (5.17) into (5.15) as

$$\eta = R - r$$
$$\cong \left[\left\{\langle M\rangle\, 3\alpha\ K(\varepsilon_p)/4b\right\}^{1/3} - 1\right] r\ . \qquad (5.22)$$

Noting that $K(\varepsilon_p)$ is a slowly varying function of ε_p and taking, for example, $K(\varepsilon_p = 0.05) \cong 1.8 \times 10^{-3}$, we see from Equation (5.22) that η is approximately constant and equal to the particle radius.

It can be concluded from the above discussion that the continuum model can predict the overall values of back stress fairly accurately in the strain ranges in which secondary slip occurs profusely--that is above ~1% plastic strain for large particles in spheroidized carbon steels.

5.3 The Role of Subgrain Boundaries

Ashby[53] has related the yield stress of single crystal containing non-deforming particles to the number and size of the particles by a consideration of the Orowan dislocation bowing mechanism. His derived expression for the yield stress, in shear, is

$$\tau_y = \tau_0 + A\mu^M b N_s^{1/2}\ \ln(2r_s/r_0)\ , \qquad (5.23)$$

where A has the value $1/2.36\pi$ or $1/2.36\pi(1-\nu)$ for edge and screw dislocations respectively, μ^M is the matrix shear modulus, N_s is the number of particles intersecting a unit area of slip plane, r_s is defined as $(2/3)^{1/2}r$ and r_o is the inner cut-off radius. Converting Equation (5.23) to a tensile stress-tensile strain relation for polycrystals, the modified Orowan equation can be stated in the form

$$\sigma_y = \sigma_0 + \left\{0.83\langle M\rangle\, b\mu^M/2\pi(1-\nu)^{1/2}\right\}\left\{1/\lambda_{sg}\right\}\ \ln(2r_s/r_0)\ . \qquad (5.24)$$

In Equation (5.24), the relation between f and N_s,

$$f = 2\pi r_s^2 N_s/3 \tag{5.25}$$

was used and λ_{sq} was defined as $(\pi/f)^{1/2}r_s$. A previous work has interpreted the lower yield stresses of spheroidized carbon steels on the basis of the Orowan model [65]. The yield stresses of tempered steels, however, do not follow Equation (5.24), they instead obey the following Hall-Petch type relation in which $\lambda_{\ell,p}$ have been used as a structural parameter (Figure 5.8),

$$\sigma_y = 13.5 + 59.7\ \lambda_{\ell,p}^{-1/2}\ . \tag{5.26}$$

However, even with this correlation, it is still not clear whether the subgrain boundaries act as barriers to dislocation motion or instead act as dislocation sources, since the Hall-Petch relation for the yield stress has been rationalized for both cases. In other words, subgrain boundaries may contribute to the flow stress by acting as barriers to glide dislocations, in which case we expect that the subgrain boundaries will give rise to internal stresses. On the other hand, they may simply act as an array of forest dislocations and provide added frictional-like resistance to glide dislocations. The mode of behavior is, in general, believed to depend on both the nature of substructure and the extent of carbon segregation to subgrain boundaries in iron based alloys [43]. To understand the role of particle pinned subgrain boundaries in spheroidized steels, the measured values of internal stresses in spheroidized carbon steels with and without subgrain boundaries were compared. For this comparison, the particle size and the grain size in the specimens with and without sub-boundaries were maintained approximately equal (viz. the specimens AC and AT2). The results show that the internal stress values are higher in the thermally cycled specimens than in the specimens containing sub-boundaries (Figure 5.9). To compare these microstructures more clearly, the unrelaxed portions of the total plastic strain estimated from the measured values of internal stresses and from the relation

$$\varepsilon_p^{u} = ((1-f)/3\mu\alpha f)\ \sigma^{i} \tag{5.27}$$

are plotted as a function of plastic strains in Figure 5.10. The maximum values of unrelaxed plastic strains are ~ 3.1×10^{-3} and ~ 2.75×10^{-3} in specimens AC and AT2, respectively. Then the maximum shear stresses at the interface, where we consider the secondary slip will start to occur, are found to be approximately $\frac{\mu}{300}$ in AC and $\frac{\mu}{330}$ in AT2. This suggests that the subgrain boundaries in spheroidized steel assist plastic relaxation and therefore lower the critical stress level to enhance plastic relaxation. It is clear now that subgrain boundaries do not contribute to internal stress and that they rather act as sources of dislocations to help reduce the residual internal stresses around particles. Furthermore, the cyclic stress-strain curves (Figure 5.11) for a thermally cycled and a tempered specimen provide additional confidence for the above point of view. Both specimens have reached an initial saturation value in about 8 cycles. The specimen AT2 exhibits cyclic softening behavior both in the tension and compression portions of the cycle, while the specimen AC shows softening in compression but with the saturated hysteresis loops still above the monotonic tensile curve. This again suggests that the role of particle-pinned-subgrain boundaries is that of sources of dislocations.

However, it should be noted here that the hardening exponents (n or n') are approximately the same in both cases, although the internal stress hardening effect is lower in the tempered case. It is difficult to rationalize this fact quantitatively, so that we suggest the following qualitative explanation: According to the particle strengthening model discussed previously in Section 3.4, the flow stresses are composed of the back stress effects and the forest type hardening effect caused by the secondary dislocations generated during plastic relaxation. The forest stress has been shown to be proportional to the density of secondary dislocations in Equation (3.28). If the subgrain boundaries assist the relaxation of Orowan loops, then the secondary dislocation density will be increased and this process essentially lowers the internal stress. Thus, it is suggested from the similar hardening exponents in both the tempered and the cycled specimen that the back stress hardening effects and the forest hardening effect may compensate each other to produce a similar overall strain-hardening behavior, with the further understanding that the tempered specimens will have lower values of the Hollomon constant k_1 and k'_1. After attaining the saturation values of internal stress, the forest hardening effects will control strain-hardening behavior. Table 4.3 shows that the tempered specimen, AT2, again has a higher hardening index than the cycled one, AC, which is consistent with the previous discussion.

5.4 Strain-Hardening Behavior in Spheroidized Carbon Steel

5.4.1. "Double-n" Strain-Hardening Behavior

Morrison [66] has observed the transition in the strain-hardening behavior of low carbon steels at a strain of ~ 8% and loosely attributed this transition to the formation of well defined cell walls and the possible easier motion of dislocations in the cell structure than in the homogeneously distributed dislocation structure. Liu and Gurland [9] also observed the "double-n" hardening behavior in spheroidized medium and high carbon steels with a transition occurring at approximately 4% strain. They explained it as follows: The rapid entaglement of strain generated dislocations initially gives larger values of n--after the transition strain, a particle pinned dislocation cell structure forms and governs the strain-hardening behavior with lower value of n. Since the above explanations both fail, to ellucidate the transition behavior in spheroidized carbon steels, which already contain the dislocation subgrain boundaries even before deformation, Anand and Gurland [67] have recently attempted to explain this transition in terms of the internal stress development at the particle-matrix interface during the first few percent of plastic deformation. The values of internal stresses, however, were estimated by taking the differences of the Hall-Petch constants, σ_{0f}, for the pure iron and the spheroidized carbon steel. This will ignore dislocation interactions. The directly measured values of internal stresses of the present study are plotted in Figure 5.9 together with the estimates of Anand and Gurland [67]. It is seen that the estimated values are a factor of 2 ~ 5 higher than the measured values. This, we consider, is a natural consequence of ignoring the interactions between the primary dislocations and the secondary dislocations generated by plastic relaxation. To see the direct relation between the internal stresses and the transition behavior, the flow stresses and the internal stresses are plotted on a log-log scale in Figure 5.6 This shows a transition in strain-hardening behavior in the strain range of 3 ~ 5% consistent with the previous observations [9,67]. Moreover, the transition strain ranges are always coincident with the strain ranges of internal stress saturation. Thus, we conclude that the "double-n" strain-hardening behavior in both the cycled and tempered carbon steels is a direct consequence of the internal stress. A general explanation can be given as follows: The relaxed portion of the imposed plastic strain develops a plastic zone around the second phase particles extending approximately equal to the particle radius. This zone prohibits complete relaxation of the entrapped Orowan loops and thus stabilizes the localized elastic strain fields due to the unrelaxed part of the total plastic strain. The resulting stresses increase rapidly during the early stages of plastic flow, that is below strains of 3 ~ 5% in spheroidized carbon steels, and accordingly give rise to an initially higher hardening exponent n. After these internal stresses reach a certain saturation level, only the "forest type" strain-hardening will continue and this is characterized by a lower hardening exponent than when both back stress and forest hardening contribute together.

5.4.2 Addition of Flow Stress Contributions

As we have already discussed, the contributions to strain-hardening in a dispersion strengthened material consist of internal stress, σ^i, "source-shortening" stress, $\Delta\sigma^{ss}$, "forest stress", σ^f, and finally the stress due to "statistical dislocation" density, $\Delta\sigma^s$. The internal stress was found to be in the form

$$\sigma^i = 3\delta\alpha\mu(f/1-f)(\varepsilon_p^{0.3}/r^{0.7}) \tag{5.28}$$

where δ is a constant.

Noting the relation $f = \frac{2\pi r^2}{3\Lambda^2}$ using $T = 1/2\mu b^2$, $\Delta\sigma^{ss}$ now can be written as

$$\Delta\sigma^{ss} = (3\mu b f/\pi r)\left[\left\{2\langle M\rangle r\varepsilon_p^u/b\right\}^{1/2} - 1\right]. \quad (5.29)$$

It seems reasonable to assume that $\Delta\sigma^s$ is given by the work-hardening increment of pure iron. One of the major difficulties, however, in describing strain-hardening behavior is in determining just how to superimpose the various hardening contributions. The most common assumption is to ignore interactions and to sum the contributions linearly to obtain

$$\sigma = \sigma_1 + \sigma_2 + \cdot \cdot \cdot \cdot + \sigma_n . \quad (5.30)$$

Koppenaal and Kuhlmann-Wilsdorf [68], on the other hand, have proposed a mean-square-root addition law, i.e.,

$$\sigma^2 = \sigma_1^2 + \sigma_2^2 + \cdot \cdot \cdot \cdot + \sigma_n^2 . \quad (5.31)$$

for the case where the various obstacles to glide dislocations have a similar strength [69]. A previous study on spheroidized carbon steel explored the use of the first assumption of linear additivity [10], but, as we noted earlier, the estimated values for, as an example, internal stress that were obtained using this assumption show a significant discrepancy with the presently measured values of internal stresses. This was attributed to the neglect of interactions between the various hardening contributions. This author feels that for the present case the mean-square-root addition law is the more reasonable, as is now explained.

Firstly, we note that since all the glide dislocations sample the long-range internal stresses, σ^i can be added linearly to the flow stress. If we assume that the other three contributions interact mutually, we may then write the hardening increment, $\Delta\sigma_h$, in the form

$$\Delta\sigma_h = \sigma_f - \sigma_{\varepsilon_p=0}$$
$$= \sigma^i + \left[(\Delta\sigma^s)^2 + (\sigma^f)^2 + (\Delta\sigma^{ss})^2\right]^{1/2} . \tag{5.32}$$

In Equation (5.32), $\sigma_{\varepsilon_p = 0}$, instead of the lower yield stress σ_y, is taken to define the hardening increment, because σ_y is generally affected by transient hardening effects associated, for example, with initial dislocation locking. To demonstrate the validity of Equation (5.32), the measured values of the flow stress were compared with the values estimated by Equation (5.32). In the process of computing σ_f, $\Delta\sigma^s$ was obtained from the work of Morrison[66] and $\Delta\sigma^{ss}$ was computed from Equation (5.29). Since the "forest stress" does not depend on the plastic zone volume and shape, we can still use Equation (3.37) to estimate σ^f. According to Ashby, $\lambda^G = \frac{r}{f}$ and λ^G, for the tempered specimens, was found to be equivalent to $\lambda_{\ell,p}$ in the Hall-Petch equation for the lower yield stress; thus, we may compute σ^f by writing

$$\sigma^f = c'\mu \langle M\rangle^{3/2} (b\varepsilon_p/\lambda_{\ell,p})^{1/2} . \tag{5.33}$$

All the results for specimen AT2 are contained in Table 5.1 and σ_f (computed) is plotted in Figure 5.12 along with σ_f (experimental). The very good correspondence between σ_f (computed) and σ_f (experimental) supports the use of Equation (5.32) for the tempered specimen. A similar process was carried out for the thermally cycled specimen AC except that we now take $\langle M\rangle = 2$ instead 2.733 to estimate σ^f by Equation (3.37)--the rational for this was discussed in Section 3.4.1. The results are included in Table 5.2 with σ_f(experimental). If we bear in mind the uncertainty in the value of the constant h, Figure 5.12 again shows good agreement with the addition law expressed in Equation (5.32). It then seems that Equation (5.32) can be applied with reasonable precision to both the tempered and the cycled carbon steels to predict the flow stress level.

5.5 Cavity Formation at Particle-Matrix Interface

One other important aspect of the internal stresses that have just been described is that they seem to contribute to the formation of cavities. Decohesion along particle-matrix interfaces is suspected to occur when the maximum normal stress at the interface exceeds some assumed fracture stress [70] (i.e. a stress criterion) or when the elastic strain energy stored during plastic deformation exceeds the energy of the new surfaces formed by cavitation (i.e. energy criterion) [71,72,73]. The stress criterion is believed to be more plausible in the case of large particles for which the energy criterion is always satisfied. The maximum interfacial normal stress is obtained from Equation (5.8) as

$$\sigma_{nn}^{max} = 2\mu\alpha\varepsilon_p^u \ . \tag{5.34}$$

However, plastic relaxation occurs from the beginning of plastic deformation, as we discussed earlier in Section 3.4.2. Thus, there will be other contributions which arise from the interactions among the secondary plastic zones of neighboring particles. Ashby [47] has computed the stresses caused by these kinds of interactions by using his secondary slip model. Argon et al. [70] have further developed Ashby's simple shear model and their results show that the maximum interfacial tensile stress is about twice the boundary shear traction for the case of rigid inclusions. Since it is not the primary intent of this present work to estimate the stresses caused by particle-particle interactions, we shall just present here a brief discussion. We note that the maximum normal interfacial stress due to inhomogeneity effects, which incidently was ignored in the Ashby model, amounts to 30 ~ 40 ksi--this is equivalent to approximately half the flow stress. These values are obtained from Equation (5.34) by using the unrelaxed plastic strains as estimated from the measured internal stress. Thus, the total normal interfacial stress, σ_{nn}^{T} , can be written in the approximate form

$$\sigma_{nn}^{T} = \sigma_{f}(\varepsilon) + \sigma_{nn}^{max} + \sigma_{int}(\varepsilon) \quad , \qquad (5.35)$$

although the stress caused by particle-particle interaction, $\sigma_{int}(\varepsilon)$, has obviously to be determined by further study. According to Equation (5.8), σ_{nn}^{max} occurs at the x_3 pole of particle (see Figure 3.3.b). The optical micrograph of Specimen AT2 (Figure 5.13.a) shows cavities formed at such poles together with particle shearing. It is found that σ_{nn}^{max} decreases with increasing particle size(i.e. 23 ksi-AT3, 32 ksi-AT2, and 38 ksi-AT1). This then implies that the interfacial normal stresses of large particles can be relieved to a greater extent than in the case of small particles. Thus, it is suggested that large particles tend to be sheared, whereas small particles develop cavities in the tensile direction at the particle-matrix interface. Figure 5.13.b clearly supports this explanation, because it shows only the cavities formed at the poles of particles in the tensile direction. This observation also suggests the validity of the particle strengthening model illustrated in Figure 3.3.b. Further analytic and experimental work is required to obtain reliable estimates of the interfacial stresses caused by particle-particle interactions. This together with the present work, we hope, will enable us to predict cavity formation more clearly.

6. CONCLUSIONS

1. Internal Stress

The residual internal stresses developed around the second phase particles are caused by plastic incompatibilities between the elastic particles and the elastic-plastic matrix. These stresses give rise to the large Bauschinger effects observed in the present experiments. The continuum model, based on the assumption of multiple slip, predicts that the magnitude of these internal stresses is given by the relation,

$$\sigma^{i} = 3\delta\alpha\mu(f/1-f)(\varepsilon_p^{0.3}/r^{0.7}) .$$

The predicted values are in a good agreement with the measurements provided that secondary slip occurs profusely. The back stress hardening contributions were found to reach approximately 20% of the total work-hardening in spheroidized carbon steels. The model further suggests that there exists the locally fluctuating stresses which fall off inversely with the 3rd power of distance from a particle. It was further found that the so-called secondary plastic zone extended a distance from the particle interface approximately equal to the particle radius.

2. "Double-n" Strain-Hardening Behavior

The transition in power law strain-hardening behavior of spheroidized carbon steels from a larger to a reduced value of the index n occured in the plastic strain range of 3 ~ 5% in which the internal stresses were found to reach a certain saturation level. The initially higher value of hardening exponent is caused by the combined long-range internal stress and the shortrange forest stress. When the internal stress saturates only the forest stress continues to increase thus accounting for the lower hardening exponent. It therefore can be concluded that the internal stress is directly responsible for the transition in strain-hardening behavior of spheroidized carbon steels.

3. The Nautre of Subgrain Boundaries

The internal stresses in the specimens containing subgrain boundaries were lower than in the specimens without subgrain boundaries. That is, the existence of subgrain boundaries lowered the critical stress, τ^*, required to start the secondary slip process. τ^* was found to be approximately $\frac{\mu}{330}$ in AT2 and $\frac{\mu}{300}$ in AC. The cyclic stress-strain curves also suggest that the subgrain boundaries, formed by heat treatment in carbon steels, act as sources for dislocations. Furthermore, they assist in the process of relaxation of entrapped Orowan loops and thus lead to a reduction in the maximum internal stress level.

4. Flow Stress Contributions

In dispersion strengthened alloys, there was found to be four hardening contributions, viz. (1) internal stress, σ^i; (2) "source-shortening" stress, $\Delta\sigma^{ss}$; (3) "forest stress", σ^f; and (4) the stress arising from dislocation in relaxation zone, $\Delta\sigma^s$. Among the several addition laws, the equation

$$\sigma_f = \sigma_{\dot{\varepsilon}_p=0} + \sigma^i + \left[(\Delta\sigma^s)^2 + (\Delta\sigma^{ss})^2 + (\sigma^f)^2\right]^{1/2}$$

showed good agreement with the experimental flow stress curves of both tempered and thermally cycled carbon steels.

5. Cavity Formation at Particle-Matrix Interfaces

The maximum normal interfacial stress occurs in the tensile direction at the poles of particles. It was also found that σ_{nn}^{max} depends upon the particle size. The values for σ_{nn}^{max} of 23 ksi, 32 ksi, 38 ksi, and 40 ksi for specimens AT3, AT2, AT1, and AC, respectively were found. We suggest that the total interfacial normal stress, σ_{nn}^{T}, can be written as

$$\sigma_{nn}^{T} = 2\mu\alpha(\varepsilon_p^{u})^{max} + \sigma_f(\varepsilon) + \sigma_{int}(\varepsilon) .$$

ACKNOWLEDGEMENTS

The author wishes to express his sincere gratitude to Professor Robert J. Asaro for his guidance and patience throughout the course of this research. He also expresses his thanks to Professor Joseph Gurland for his helpful discussion on this research. Special thanks are also expressed to Mr. H.J. Stanton for his kind assistance in the experimental work.

This work was supported by the U.S. Energy Research and Development Agency under Contract EY-76-S-02-3084.

REFERENCES

1. R.L. Wooley: Phil. Mag., 1953, Vol. 44, P. 597.
2. E. Orowan: Internal Stresses and Fatigue in Metals, P. 59, Elsevier, 1959.
3. R.J. Asaro: Int. J. Engin. Sci., 1975, Vol. 13, P. 271.
4. R.J. Asaro: Acta Met., 1975, Vol. 23, P. 1255.
5. M. Mroz: J. Mech. Phys. Solids, 1967, Vol. 15, P. 163.
6. K. Tanaka and T. Mori: Acta Met., 1970, Vol. 18, P. 931.
7. L.M. Brown and W.M. Stobbs: Phil. Mag., 1971, Vol. 23, P. 1185.
8. D.W. Wilson: Acta Met. 1965, Vol. 13, P. 807.
9. C.T. Liu and J. Gurland: Trans. TMS-AIME, 1968, Vol. 242, P. 1535.
10. L. Anand: Ph.D. Thesis, 1975, Brown University.
11. E.O. Hall: Proc. Phys. Soc., London, 1951, B64, P. 747.
12. N.J. Petch: J. Iron Steel Inst., 1953, Vol. 25, P. 25.
13. R.P. Carreker: Trans. TMS-AIME, 1957, Vol. 209, P. 113.
14. P. Feltham and G.J. Copley: Phil. Mag., 1960, Vol. 5, P. 649.
15. J. Hardy, J.D. Meakin, and N.J. Petch: Phil. Mag., 1962, Vol. 7, P. 45.
16. J.C.M. Li and Y.C. Chou: Met. Trans., 1970, Vol. 1, P. 1145.
17. J.C.M. Li: Trans. TMS-AIME, 1963, Vol. 227, P. 239.
18. M.F. Ashby: Phil. Mag., 1970, Vol. 21, P. 339.
19. J.P. Hirth and J. Lothe: Theory of Dislocations, P. 694, McGraw-Hill, Inc., 1968.
20. R.W. Armstrong, I. Codd, R.M. Douthwaite, and N.J. Petch: Phil. Mag., Vol. 7, P. 45.

21. F.R.N. Nabarro, Z.S. Basinski, and D.B. Halt: Advances in Physics, 1964, Vol. 13, P. 193.

22. M.F. Ashby: Strengthening Method in Crystals, P. 137, A. Kelly and R.B. Nicholson eds., John Wiley and Sons Inc., New York, 1971.

23. A.W. Thompson, M.I. Baskes, and W.F. Flanagan: Acta Met., 1973, Vol. 21, P. 1017.

24. H. Conrad, S. Feurstein, and L. Rice: Mat. Sci. and Eng., 1967, Vol. 2, P. 157.

25. G.I. Taylor: Proc. Roy. Soc., London, 1934, A145, P. 362.

26. G.I. Taylor: J.I.M., 1938, Vol. 62, P. 307.

27. J.W. Huchinson: J. Mech. Phys. Solids, 1964, Vol. 12, P. 25.

28. R. Ebeling and M.F. Ashby: Phil. Mag., 1966, Vol. 13, P. 805.

29. R.L. Jones and A. Kelly: Proc. Second Bolton Landing Conference on Oxide Dispersion Strengthening, P. 229, G.S. Ansell, T.D. Cooper, and F.V. Lenel eds., Gordon and Breach, New York, 1966.

30. R.J. McClroy and Z.C. Szkopiak: Int. Met. Reviews, 1972, Vol. 17, P. 175.

31. P.B. Hirsch: J. Inst. Metals, 1958-59, Vol. 87, P. 406.

32. A.W. Thompson: In press.

33. D.L. Holt: J. Appl. Phys., 1970, Vol. 41, P. 3197.

34. J.W. Cahn: Acta Met., 1962, Vol. 10, P. 179.

35. C.E. Feltner and C. Laird: Acta Met., 1967, Vol. 15, P. 1633.

36. G. Langford and M. Cohen: Trans. ASM, 1969, Vol. 62, P. 623.

37. J.C.M. Li: Acta Met., 1960, Vol. 8, P. 296.

38. A.N. Stroh: Acta Met., 1961, Vol. 9, P. 315.

39. H.J. Rack and M. Cohen: Frontiers in Materials Science, P. 365, Dekker, New York, 1976.

40. J.T. Moore and D. Kuhlmann-Wilsdorf: J. Appl. Phys., 1971, Vol. 42, P. 953, P. 3717, P. 3726.

41. M.N. Bassim and D. Kuhlmann-Wilsdorf: Phy. Stat. Sol. (a), 1973, Vol. 17, P. 281, P. 379.

42. M.N. Bassim and D. Kuhlmann-Wilsdorf: Phy. Stat. Sol. (a), 1973, Vol. 19, P. 335.

43. J.D. Embury: Strengthening Methods in Crystals, P. 331, A. Kelly and R.B. Nicholson eds., John Wiley and Sons, Inc., New York, 1971.

44. C. Rey and G. Saada: Phil. Mag., 1976, Vol. 33, P. 825.

45. E. Orowan: Discussion in the Symposium on Internal Stresses in Metals and Alloys, P. 451, Inst. of Metals, London, 1948.

46. T. Mori and K. Narita: Acta Met., 1975, Vol. 23, P. 85.

47. M.F. Ashby: Phil. Mag., 1966, Vol. 14, P. 1157.

48. P.B. Hirsh and F.J. Humpreys: Proc. Roy. Soc.,London, 1970, A318, P. 72.

49. J.C. Fisher, E.W. Hart, and R.H. Pry: Acta Met.,1953, Vol. 1. P. 336.

50. E.W. Hart: Acta Met., 1972, Vol. 20, P. 275.

51. A. Kelly and R.B. Nicholson: Prog. Metal Phys., 1963, Vol. 10, P. 51.

52. D.W. Wilson and Y.A. Konnan: Acta Met., 1964, Vol. 12, P. 617.

53. M.F. Ashby: Oxide Dispersion Strengthening, P. 143, G.S. Ansell, T.D. Cooper, and F.V. Lenel eds., Gordon and Breach, New York, 1966.

54. J.D. Atkinson, L.M. Brown, and W.M. Stobbs: Phil. Mag., 1974, Vol. 30, P. 1247.

55. A.H. Cotrell: The Mechanical Properties of Matter, John Wiley, 1964.

56. G. Moan, C.M. Sargent, and J.D. Embury: Proc. 3rd Int. Conf. on Strength of Metals and Alloys, P. 41, Inst. Metals and Iron and Steel Inst., 1973.

57. A. Abel and H. Muir: Phil. Mag., 1972, Vol. 26, P. 489.

58. J.D. Eshelby: Proc. Roy. Soc.,London, A241, P. 376.

59. T. Mori and K. Tanaka: Acta Met., 1973, Vol. 21, P. 571.

60. L.M. Brown and W.M. Stobbs: Phil. Mag., 1971, Vol. 30, P. 1201.

61. L.M. Brown: Acta Met., 1973, Vol. 21, P. 879.

62. E.E. Underwood: Quantitative Stereology, Addison-Wiley, Reading, Massachusetts, 1970.

63. T. Kishi and T. Tanabe: JMPS, 1973, Vol. 21, P. 303.

64. J.J. Irani: JISI, 1968, Vol. 206, P. 363.

65. W.R. Tyson: Acta Met., 1963, Vol. 11, P. 61.

66. W.B. Morrison: Trans. ASM, 1966, Vol. 59, P. 824.

67. L. Anand and J. Gurland: Acta Met., 1976, Vol. 24, P. 901.

68. T.J. Koppenaal and D. Kuhlmann-Wilsdorf: Appl. Phys. Let., 1964, Vol. 4, P. 59.

69. L.M. Brown and R.K. Ham: Strenghtening Method in Crystals, P. 9, A. Kelly and R.B. Nicholson eds., John Wiley and Sons Inc., New York, 1971.

70. A.S. Argon, J. Im, and R. Safoglu: Met. Trans. A, 1975, Vol. 6A, P. 825.

71. J. Gurland and J. Plateau: Trans. ASM, 1963, Vol. 56, P. 442.

72. K. Tanaka, T. Mori, and T. Nakamura: Phil. Mag., 1970, Vol. 21, P. 267.

73. A.R. Rosenfield: Met Rev., 1968, Vol. 13, P. 29.

74. C.M. Young and O.D. Sherby: JISI, September 1973, P. 640.

TABLE 4.1 Specimen composition (wt. %).

Steel	C	Mn	Si	P	S
A	0.83	0.04	0.07	0.006	0.01
B	1.40	0.04	0.05	0.006	0.01

* Chemical analysis by Walter M. Saunders, Inc., Providence, R.I.

TABLE 4.2 Structural parameters and yield stresses.

Specimen	r *	d *	λ_p*	L *	$\lambda_{\ell,p}$*	λ_{sq}*	f	σ_y'
A C	0.52	8.64	4.75	-	-	1.26	0.127	57.2
A T 1	0.29	-	2.66	1.51	1.32	0.70	0.127	59.8
A T 2	0.51	-	4.66	2.56	2.23	1.24	0.127	53.4
A T 3	0.97	-	8.87	4.76	4.16	2.36	0.127	37.1
B T	0.51	-	2.51	2.0	1.57	0.76	0.214	69.9

unit; * - μm, ' - ksi.

TABLE 4.3 Constants of the Hollomon-type equations, $\sigma = k\epsilon^{n}$ and $\sigma = k'\epsilon_p^{n'}$, and the stresses at zero plastic strain, $\sigma_{\epsilon_p = 0}$.

Specimen	$\sigma_{\epsilon_p=0}$*	n_1	k_1*	n_2	k_2*	n'_1	k'_1*	n'_2	k'_2*
A C	35.2	0.228	164.0	0.147	127.5	0.216	159.2	0.143	126.7
A T 1	41.6	0.204	159.4	0.144	131.2	0.184	151.2	0.143	131.8
A T 2	30.9	0.229	150.1	0.163	123.1	0.21	142.6	0.167	125.0
A T 3	21.0	0.25	129.1	0.163	97.5	0.24	126.1	0.162	98.1
B T	46.7	0.268	265.8	0.133	165.7	0.266	278.8	0.130	166.0

* ; unit - ksi.

TABLE 5.1 Calculated values of $\Delta\sigma^{ss}$, $\Delta\sigma^{s}$, σ^{f}, and σ_f for specimen AT2 .

ϵ_p	σ^i measured	$\Delta\sigma^{ss}$ eq.5.29	$\Delta\sigma^{s*}$	σ^{f**} eq.5.33	σ_f^{***} computed	σ_f experiment
0.01	4.1	3.31	12.44	13.24	53.5	55.0
0.015	5.2'	3.89	14.41	16.22	58.2	59.0
0.02	6.0'	4.28	16.21	18.73	62.1	62.6
0.025	6.5'	4.53	17.73	20.94	65.2	65.6
0.028	6.9	4.65	18.88	22.16	67.3	67.6
0.035	7.1'	4.82	20.25	24.78	70.4	70.5
0.039	7.1	4.94	21.45	26.15	72.2	72.3
0.045	7.2'	4.94	22.64	28.1	74.6	74.5
0.05	7.3	4.94	23.56	29.6	76.4	76.2

' ; obtained from Fig. 5.9.

* ; $\Delta\sigma^{s}=\sigma^{s}_{\epsilon_p}-\sigma^{s}_{\epsilon_p=0}$, $\sigma^{s}_{\epsilon_p}=72.03\,\epsilon_p^{0.32}$, and $\sigma^{s}_{\epsilon_p=0}$=4.06 ksi for a 280 μm grain size "Ferrovac-E" iron[10,66].

** ; c'=0.25, μ =11.25 x 10^6 psi, $\langle M\rangle$ =2.733 and b=2.42 Å.

*** ; $\sigma_{\epsilon_p=0}$=30.9 ksi.

TABLE 5.2 Calculated values of $\Delta\sigma^{ss}$, $\Delta\sigma^{s}$, σ^{f}, and σ_f for specimen AC.

ϵ_P	σ^{i} measured	$\Delta\sigma^{ss}$ eq.5.29	$\Delta\sigma^{s*}$	$\Delta\sigma^{f**}$ eq.3.37	σ_f^{***} computed	σ_f experiment
0.01	5.30	4.0	12.44	11.95	58.7	59.8
0.017	7.00	4.85	15.31	15.35	64.4	65.2
0.02	7.5'	5.07	16.21	16.9	66.7	68.0
0.028	8.3	5.28	18.88	20.0	71.5	73.5
0.035	8.6'	5.39	20.25	22.36	74.4	77.0
0.038	8.65	5.44	21.24	23.3	75.8	78.0
0.045	8.8'	5.44	22.64	25.36	78.9	80.5
0.048	8.94	5.44	23.11	26.05	79.4	81.5

' ; obtained from Fig. 5.9.

* ; the same with in TABLE 5.1.

** ; $c=1/4$, $h=8$, $\langle M\rangle =2$.

*** ; $\sigma_{\epsilon_{p=0}}=35.2$ ksi.

FIGURE CAPTIONS

3.1 Wilson's construction. A schematic illustration of the relation between Bauschinger effect and permanent softening.

3.2 Elastic-plastic model which provides a theoretical basis for the relation $\sigma^{ps} = 2\sigma^{i}$. The dotted round curve is a consequence of inhomogeneous local stress.

3.3 Particle strengthening model:

(a) Dislocation loop distribution in multiple slip model.

(b) Eshelby's transformation problem equivalent to (a).

(c) FHP model.

(d) Brown and Stobbs model.

4.1 (a) Optical micrograph of thermally cycled Specimen AC: magnification 1,800 times.

(b) Two stage carbon replica electron micrograph of Specimen AC, shows that particles are contained in grain boundaries; mangification 6,000 times.

4.2 (a) Optical micrograph of Specimen AT2, quenched and tempered at 700°C for 8 hours; magnification 1,800 times.

(b) Two stage carbon replica electron micrograph of (a) reveals the particle-pinned-subgrain boundaries: magnification 6,000 times.

4.3 (a) Optical micrograph of Specimen AT3, quenched and tempered at 700°C for 40 hours: magnification 1,800 times.

(b) Replica electron micrograph reveals clearly the particle interlinked subgrain boundaries: magnification 4,000 times.

4.4 An example how the magnitude of the permanent softening is measured (for Specimen AC).

4.5 The amount of permanent softening as a function of reverse plastic strain at the given pre-plastic strains.

5.1 The variations of the stresses developed at a particle-matrix interface on the plane of $x_2 = 0$. The polar plot of stress takes the particle boundary as the zero of stress.

5.2 Mean normal stresses in the matrix with a maximum value of $\sim 0.3\mu\varepsilon_p^u$ at $R \cong 1.3r$ and falls off as $1/R^3$.

5.3 Graphical solutions of Equation (5.16) at $\varepsilon_p = 0.03$, 0.04, and 0.05. $b = 2.42\mathring{A}$, $\nu = 1/3$, $h = 8$, $c = 1/3$, and $\langle M \rangle = 2$.

5.4 Particle size effect on internal stresses for a given volume fraction (Specimen AT, $f = 0.127$, $\varepsilon_p = 0.05$)

5.5 Graphical solutions of Equation (5.16) at $r = 0.29$, 0.51, and 0.97μm. Numerical constants are the same as in 5.3.

5.6 The relation between "double-n" strain-hardening behavior and permanent softening. The plots also suggest the relation of $\sigma^{ps} = k\varepsilon_p^m$ for quenched and tempered specimens. The transition starts to occur at the points marked by arrows.

5.7 Unrelaxed strains as a function of plastic strains. Predicted values from the continuum model show a good fit to the measured ones (Specimens AT2 and AT3).

5.8 Lower yield stresses in tempered specimens are plotted as a function of $\lambda_{\ell,p}^{-1/2}$ as a structural parameter of Hall-Petch equation.

5.9 The measured values of internal stresses are compared with the values used in a previous work of Anand and it shows that σ^i also depends on the microstructure.

5.10 Unrelaxed plastic strains computed from the measured values of internal stresses vs. plastic strains.

5.11 Cyclic stress-strain curves:

(a) for the specimen, quenched and thermally cycled

(b) and for the specimen, quenched and tempered at 700°C for 8 hours.

5.12 The experimental and the predicted flow stress curves.

5.13 Optical micrographs of the longitudinal section of:

(a) Specimen AT2, white arrows indicate cavities, formed at the particle-matrix interface. Double arrow represents tensile direction. Magnification 2,200 times.

(b) Specimen AT1. Double arrow represents tensile direction. Magnification 2,200 times.

Both specimens loaded until necking occurred.

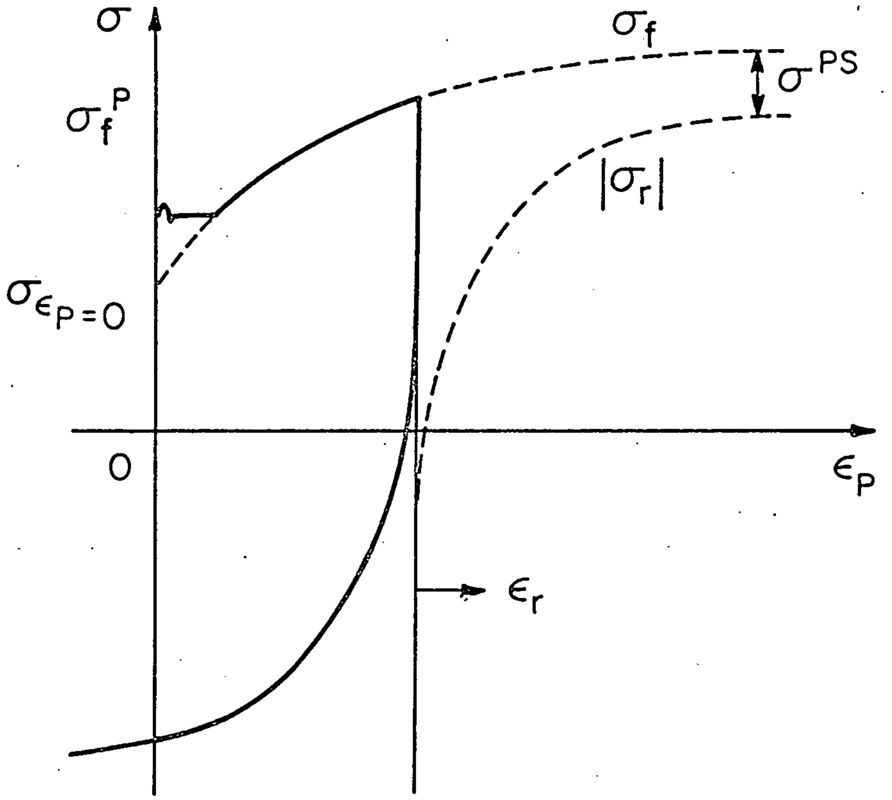

FIGURE 3.1

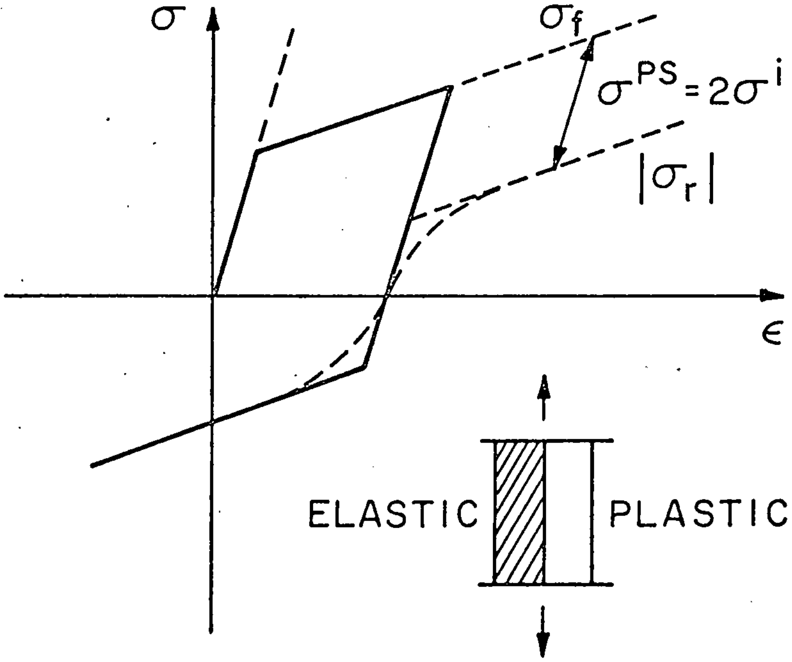

FIGURE 3.2

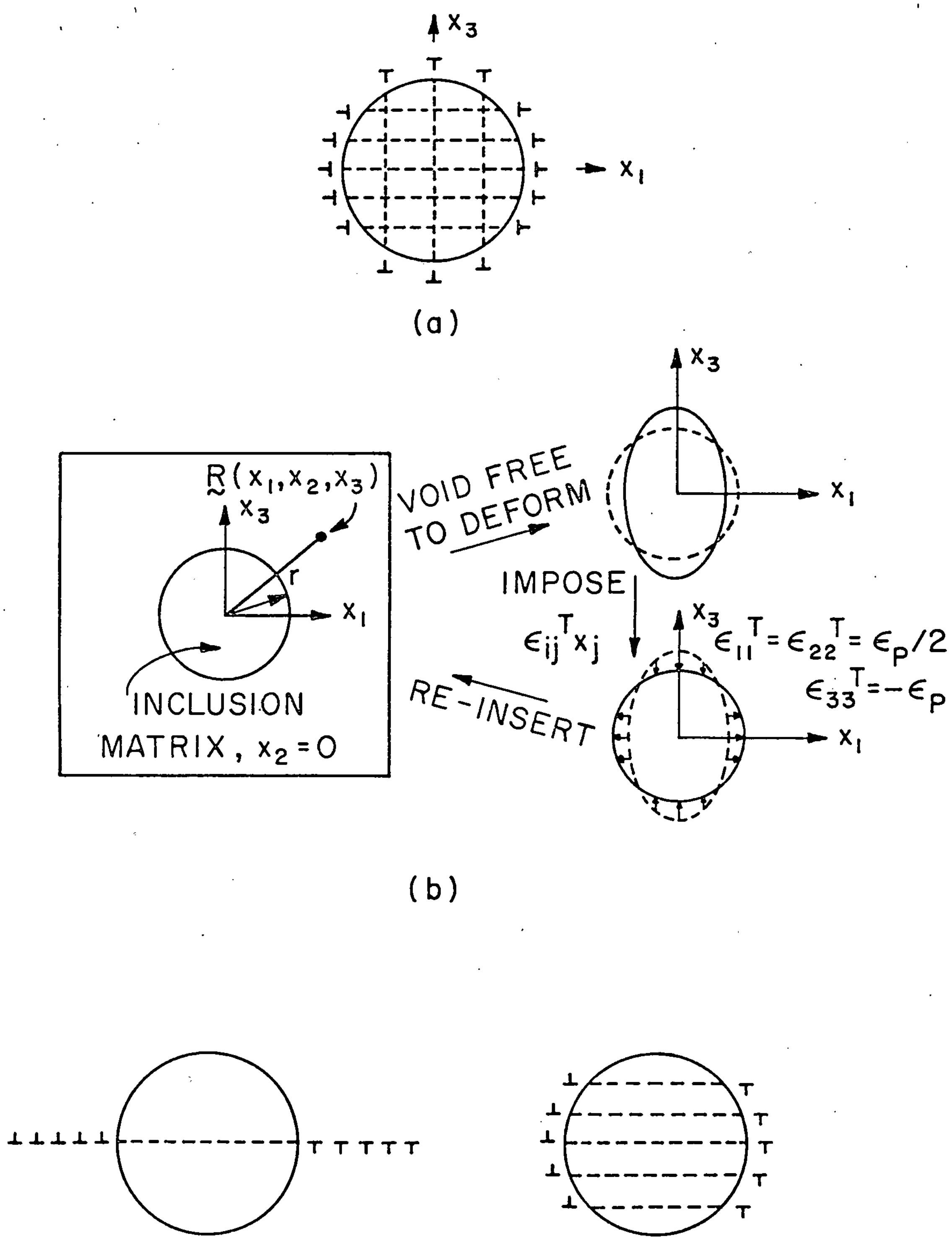

(a)

(b)

(c)

(d)

FIGURE 3.3

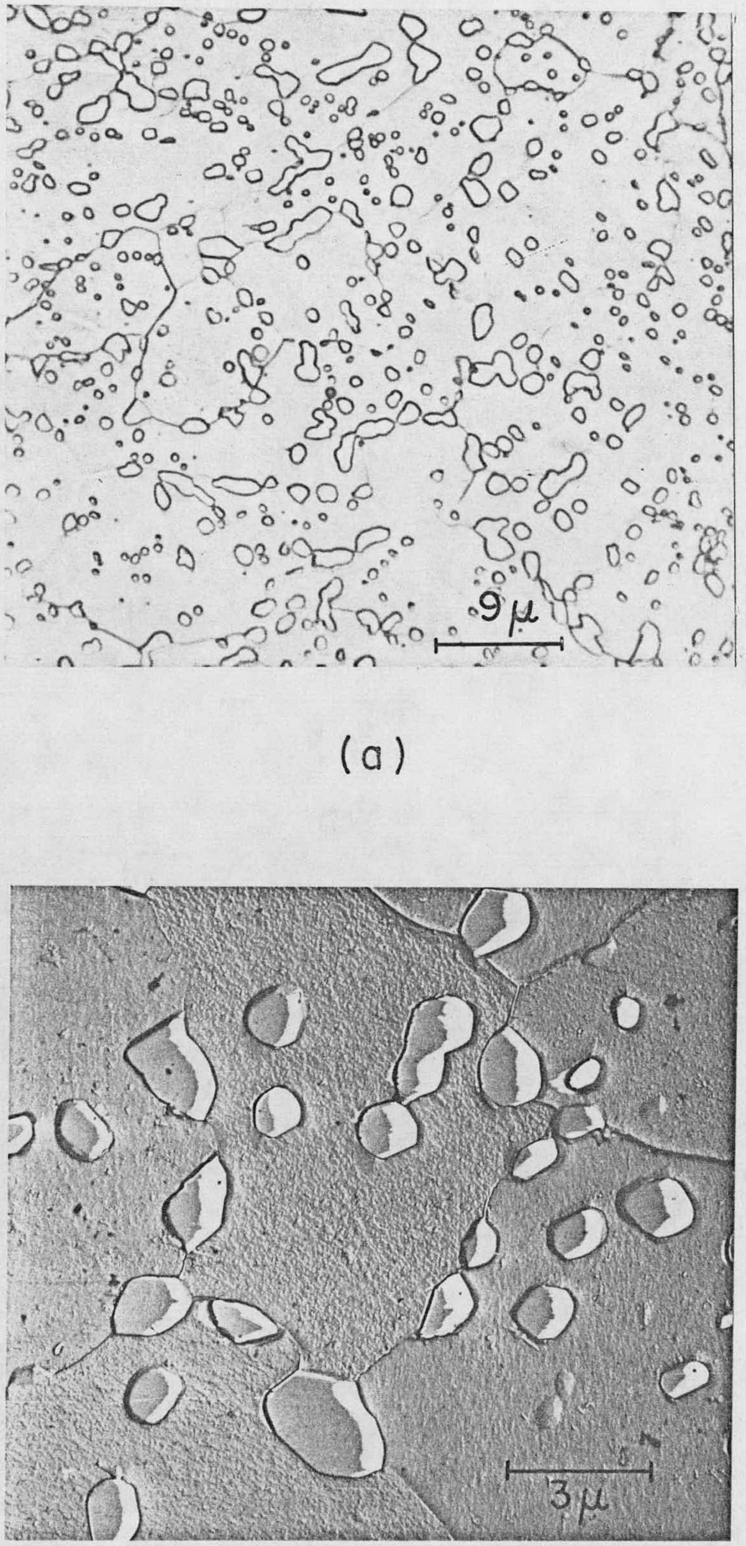

(a)

(b)

FIGURE 4.1

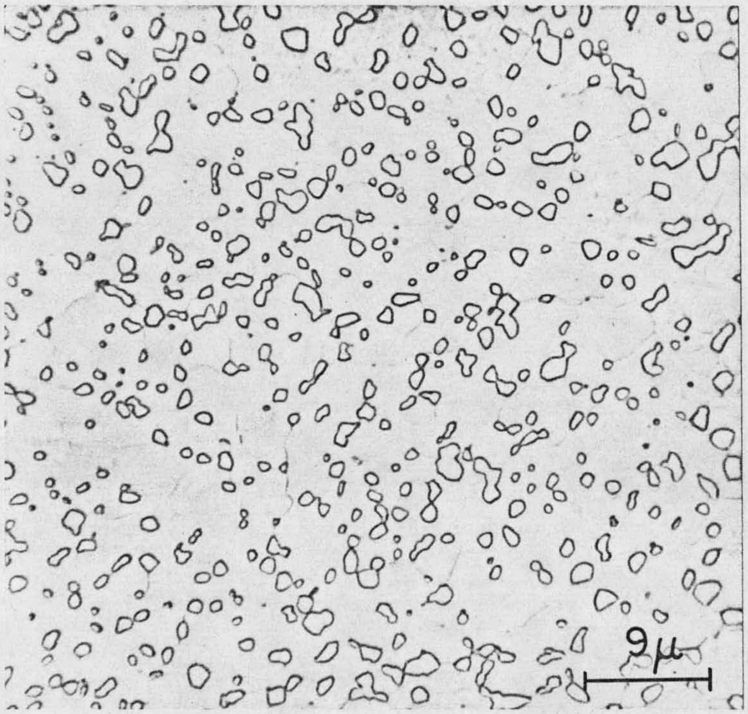

(a)

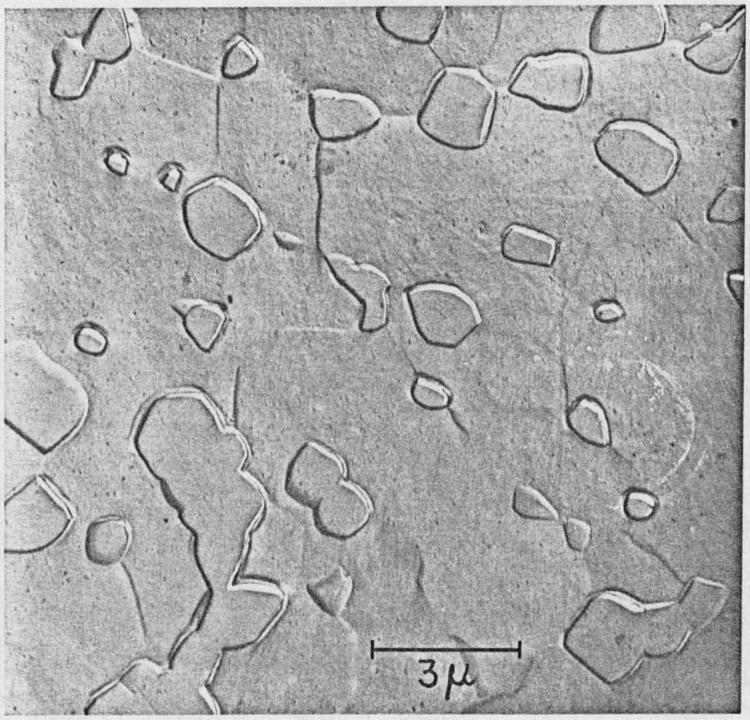

(b)

FIGURE 4.2

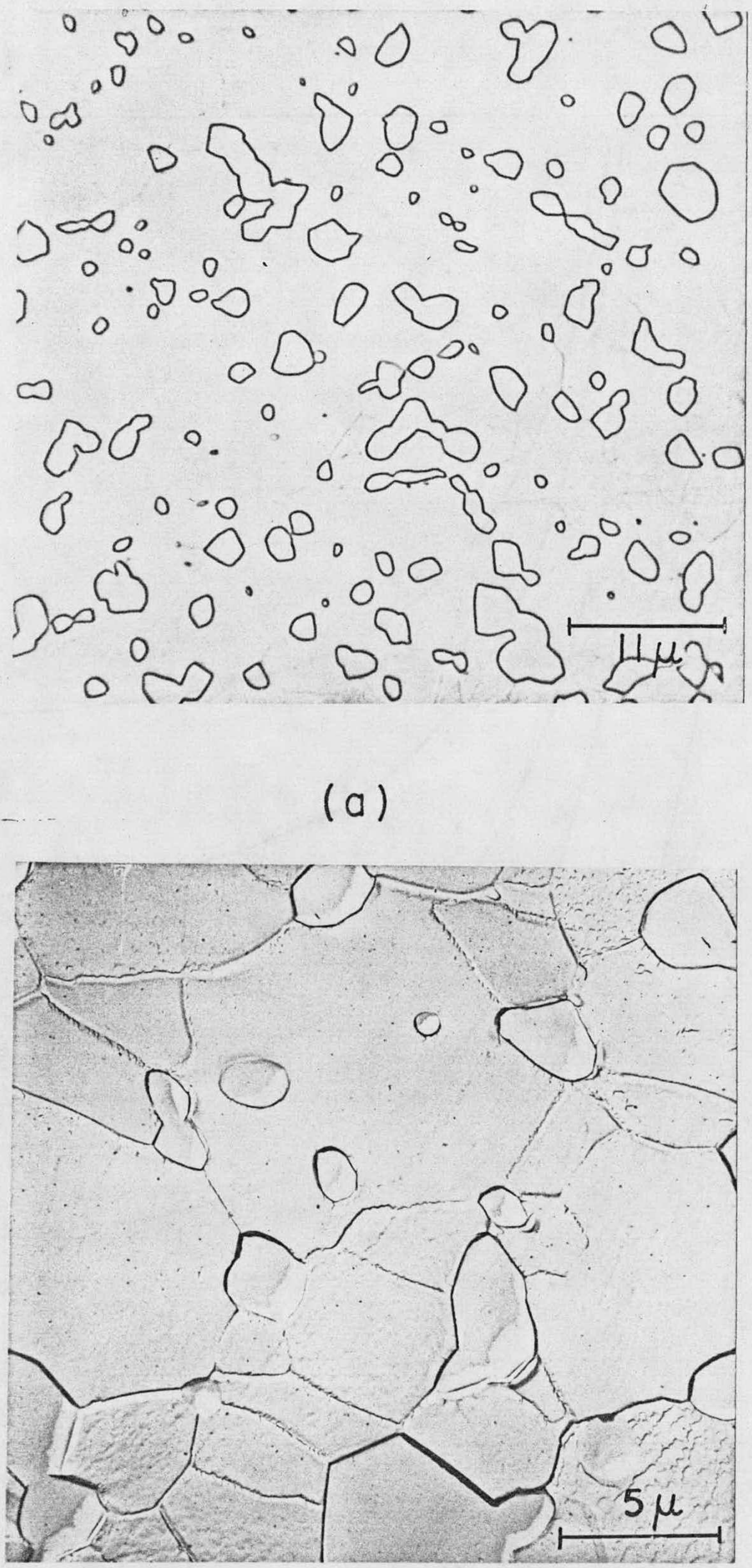

(a)

(b)

FIGURE 4.3

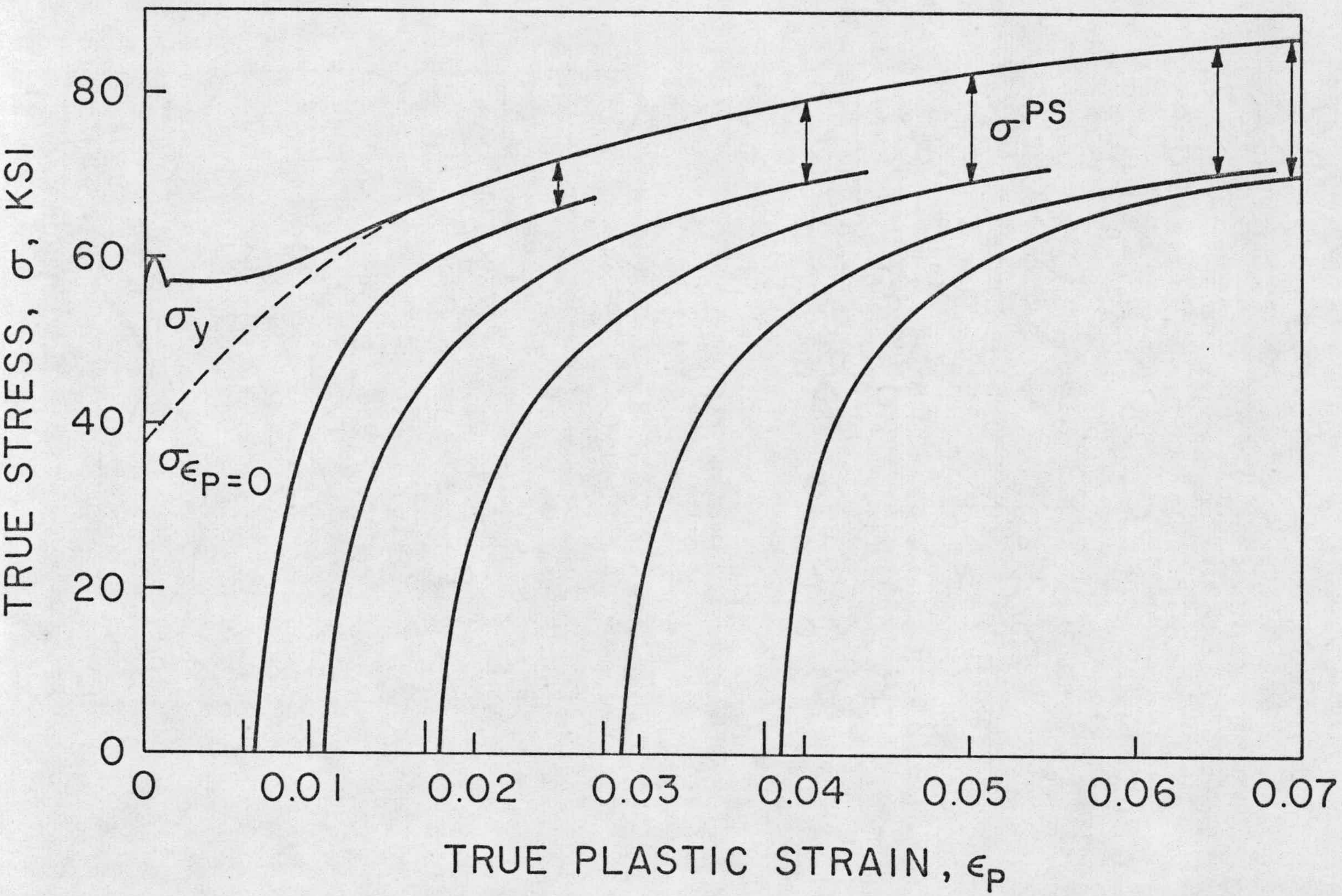
TRUE STRESS, σ, KSI
80
60
40
20
0
σ^{PS}
σ_y
$\sigma_{\epsilon_P=0}$
0
0.01
0.02
0.03
0.04
0.05
0.06
0.07
TRUE PLASTIC STRAIN, ϵ_P

FIGURE 4.4

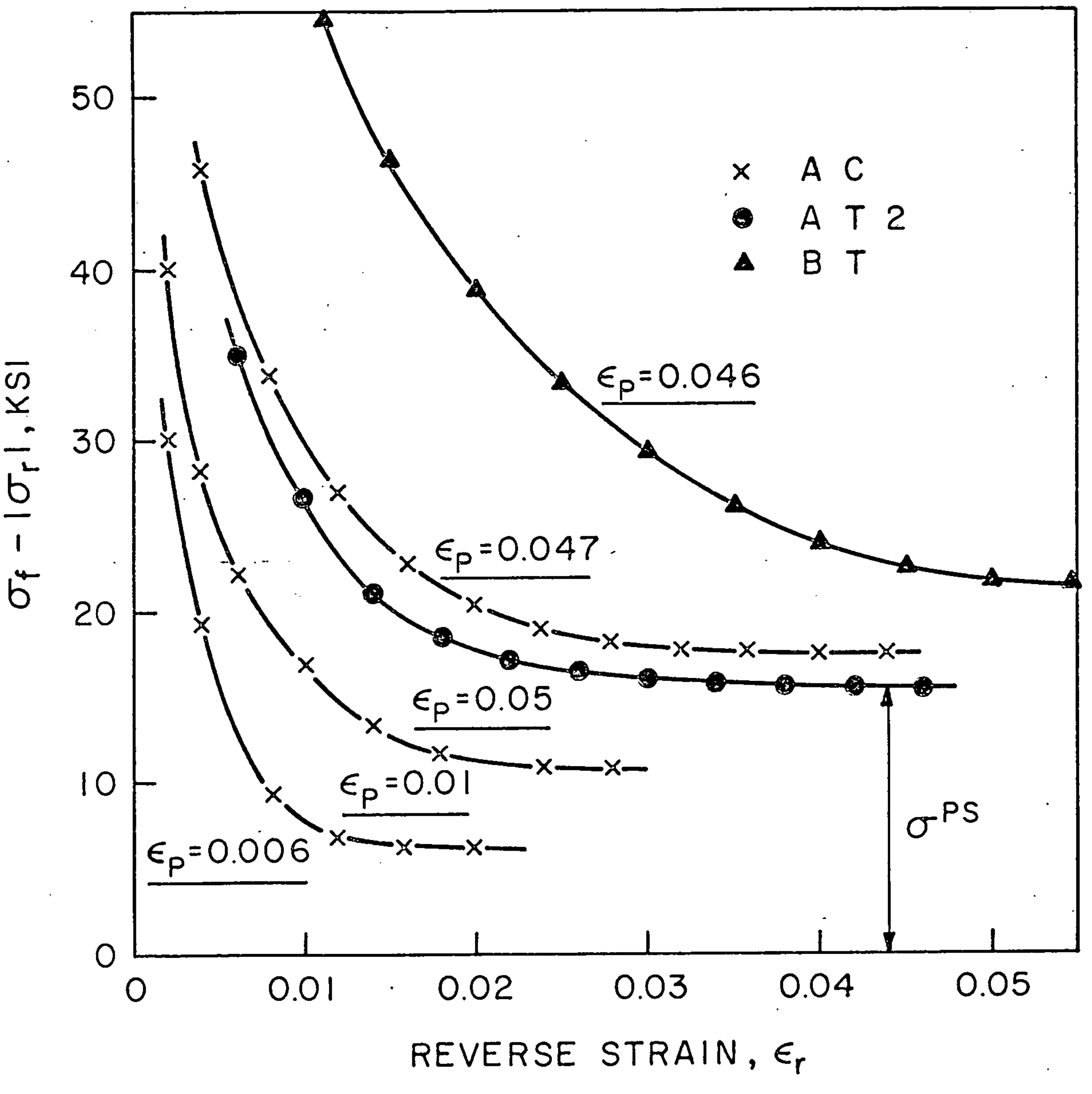
× A C
● A T 2
▲ B T
ϵ_p=0.046
ϵ_p=0.047
ϵ_p=0.05
ϵ_p=0.01
ϵ_p=0.006
σ^{PS}
$\sigma_f - |\sigma_r|$, KSI
0
10
20
30
40
50
0
0.01
0.02
0.03
0.04
0.05
REVERSE STRAIN, ϵ_r

FIGURE 4.5

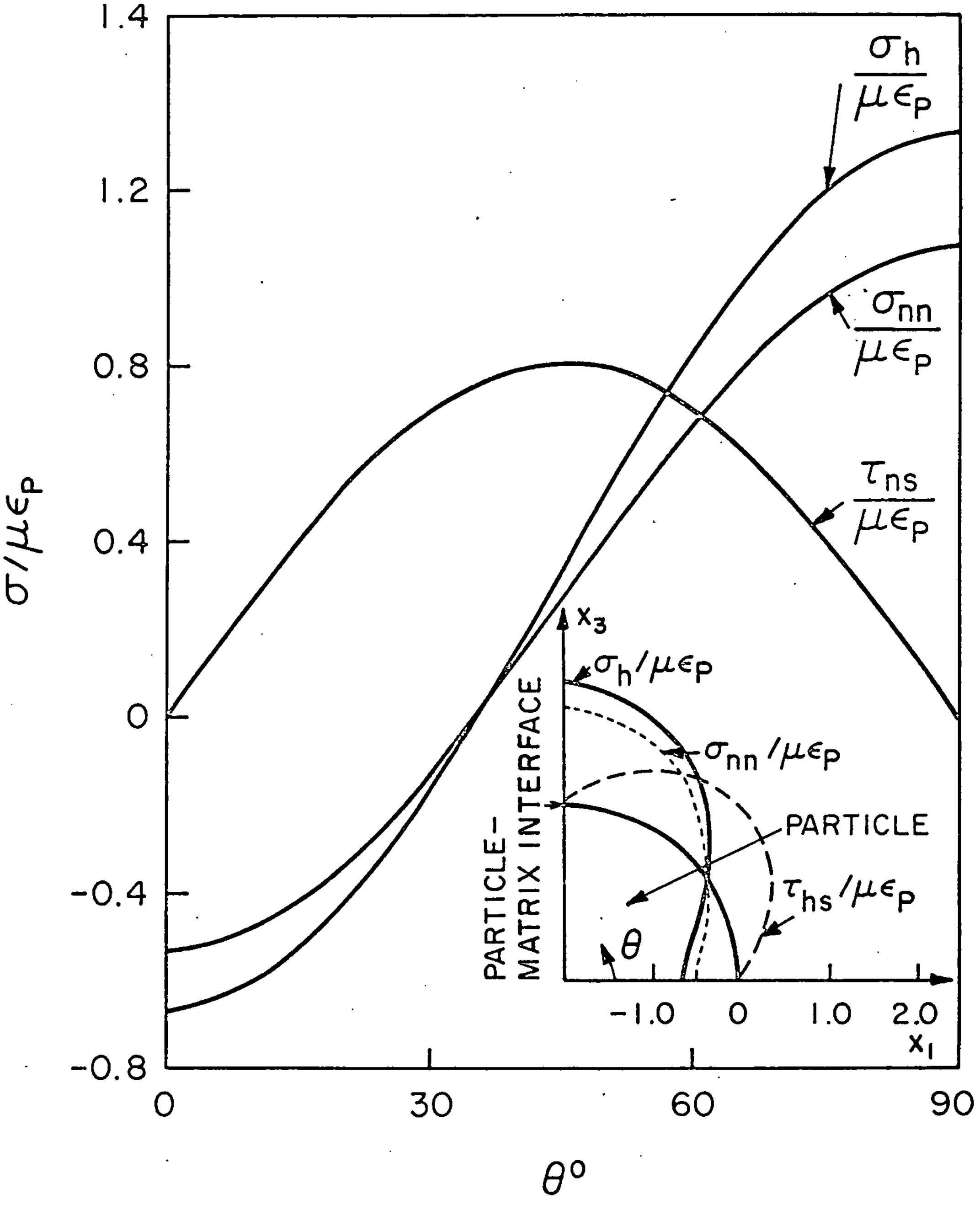
1.4
1.2
0.8
0.4
0
-0.4
-0.8
$\sigma/\mu\epsilon_P$
0
30
60
90
$\theta°$
$\frac{\sigma_h}{\mu\epsilon_P}$
$\frac{\sigma_{nn}}{\mu\epsilon_P}$
$\frac{\tau_{ns}}{\mu\epsilon_P}$
x_3
$\sigma_h/\mu\epsilon_P$
$\sigma_{nn}/\mu\epsilon_P$
PARTICLE
$\tau_{hs}/\mu\epsilon_P$
PARTICLE-MATRIX INTERFACE
θ
-1.0
0
1.0
2.0
x_1

FIGURE 5.1

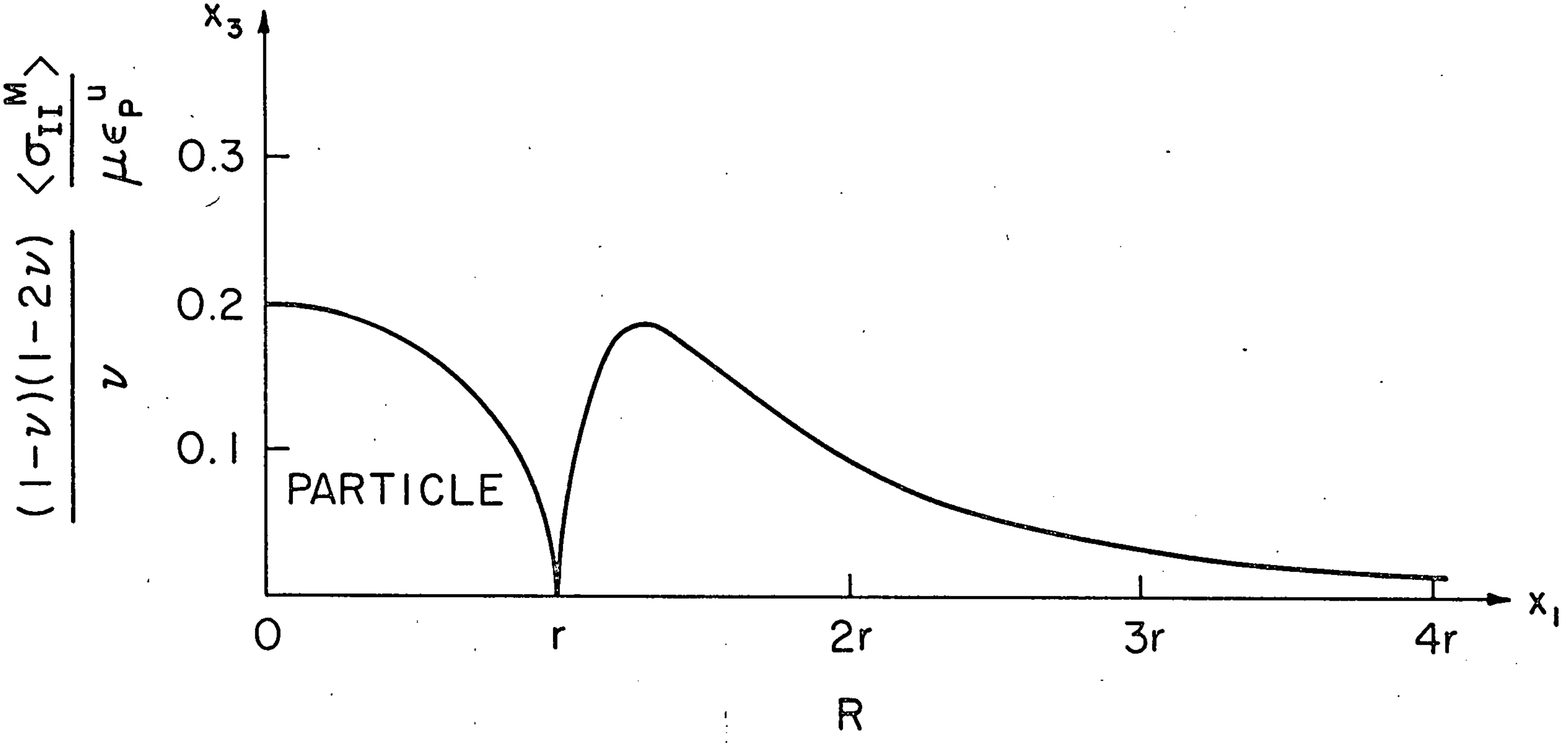
$\frac{(1-\nu)(1-2\nu)}{\nu} \frac{\langle \sigma_{II}^{M} \rangle}{\mu \epsilon_{P}^{u}}$
x_3
0.3
0.2
0.1
PARTICLE
0
r
2r
3r
4r
x_1
R

FIGURE 5.2

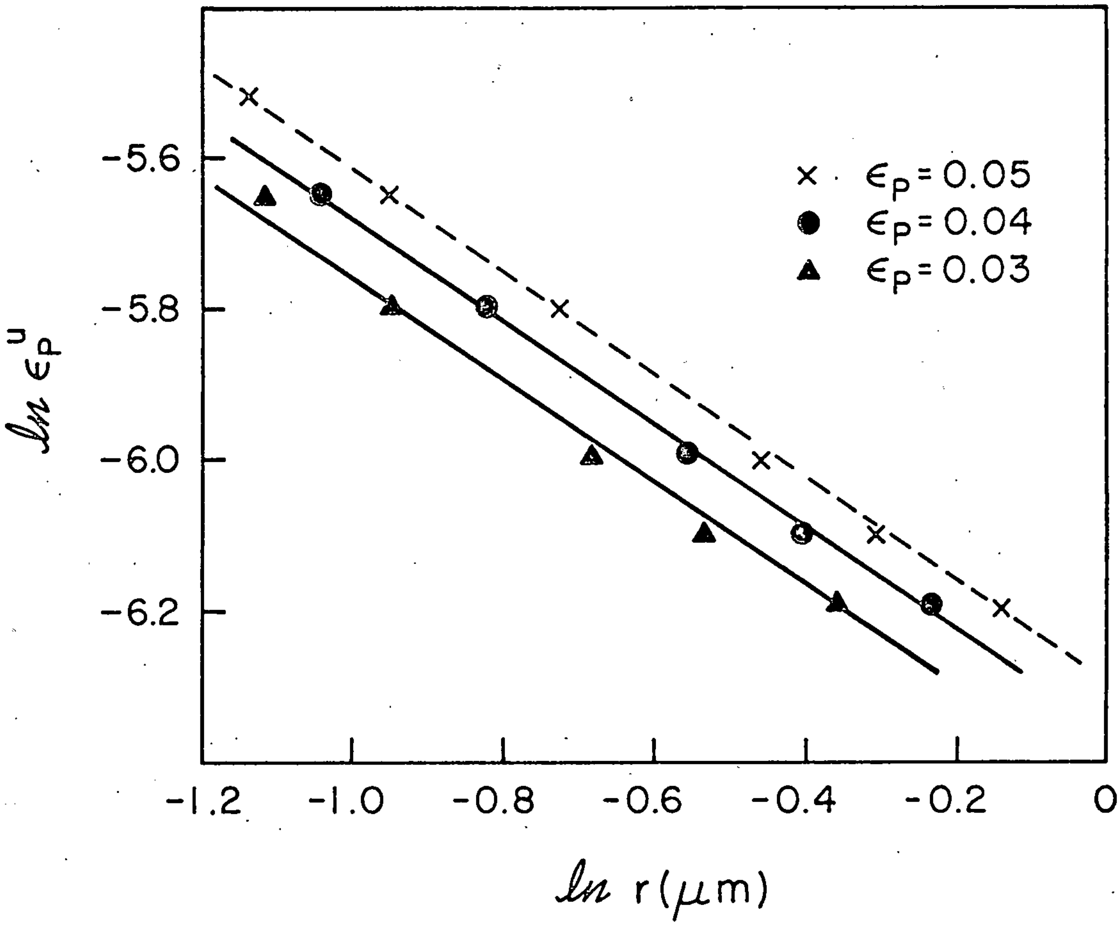
-5.6
-5.8
-6.0
-6.2
$\ln \epsilon_p^u$
× $\epsilon_p = 0.05$
● $\epsilon_p = 0.04$
▲ $\epsilon_p = 0.03$
-1.2
-1.0
-0.8
-0.6
-0.4
-0.2
0
$\ln r(\mu m)$

FIGURE 5.3

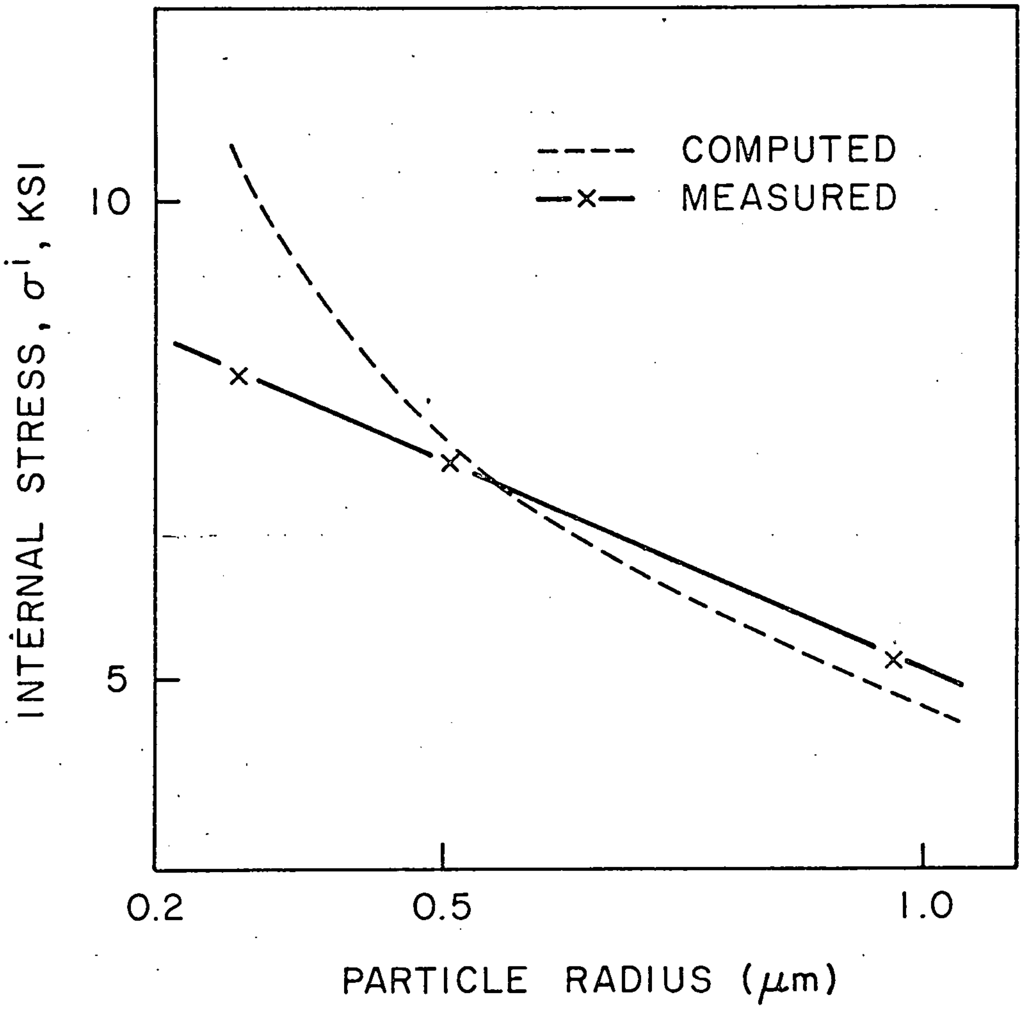

COMPUTED
MEASURED
INTERNAL STRESS, σ^i, KSI
10
5
0.2
0.5
1.0
PARTICLE RADIUS (μm)

FIGURE 5.4

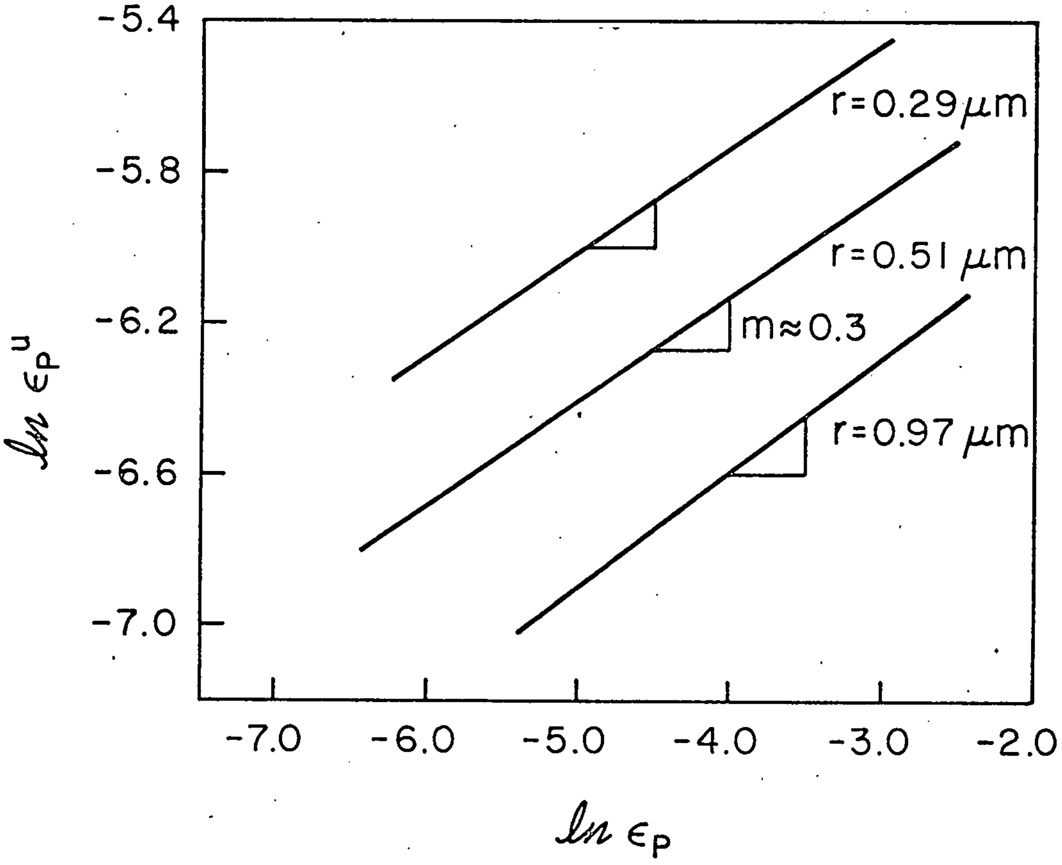
-5.4
-5.8
-6.2
-6.6
-7.0
-7.0
-6.0
-5.0
-4.0
-3.0
-2.0
$\ln \epsilon_P^u$
$\ln \epsilon_P$
$r=0.29\,\mu m$
$r=0.51\,\mu m$
$m \approx 0.3$
$r=0.97\,\mu m$

FIGURE 5.5

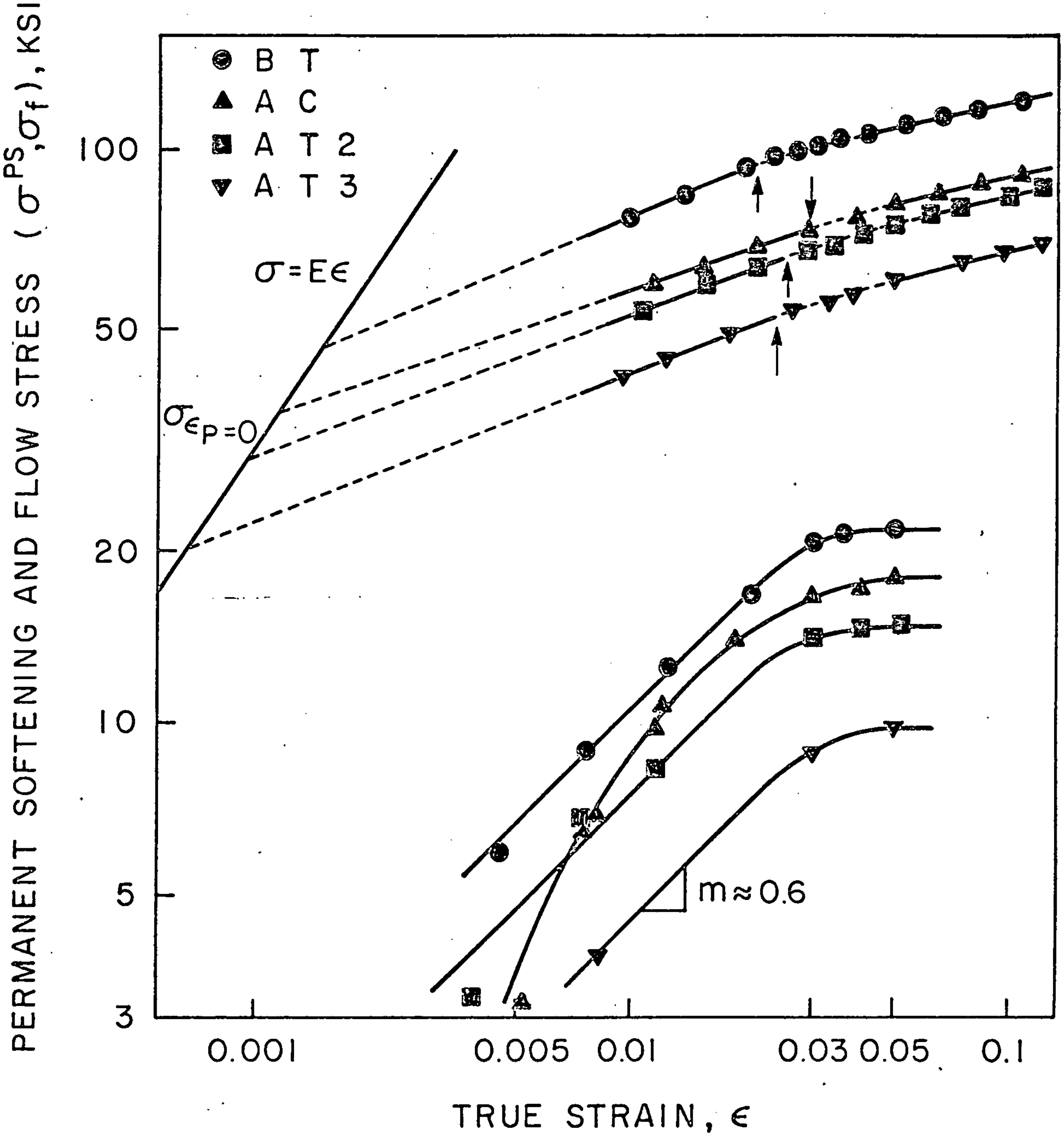
● B T
▲ A C
■ A T 2
▼ A T 3
$\sigma = E\epsilon$
$\sigma_{\epsilon_P=0}$
$m \approx 0.6$
100
50
20
10
5
3
0.001
0.005
0.01
0.03
0.05
0.1
PERMANENT SOFTENING AND FLOW STRESS (σ^{PS}, σ_f), KSI
TRUE STRAIN, ϵ

FIGURE 5.6

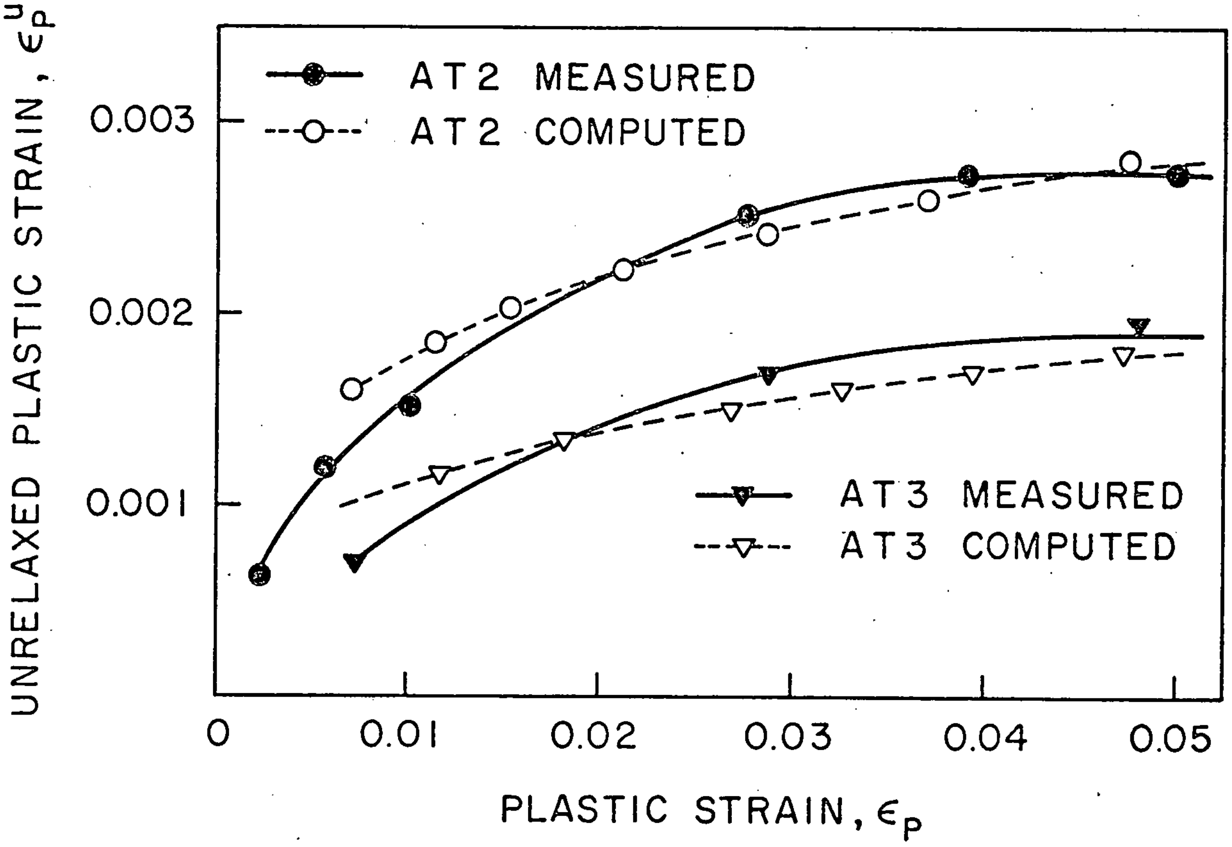
AT2 MEASURED
AT2 COMPUTED
AT3 MEASURED
AT3 COMPUTED
0.003
0.002
0.001
0
0.01
0.02
0.03
0.04
0.05
UNRELAXED PLASTIC STRAIN, ϵ_p^u
PLASTIC STRAIN, ϵ_p

FIGURE 5.7

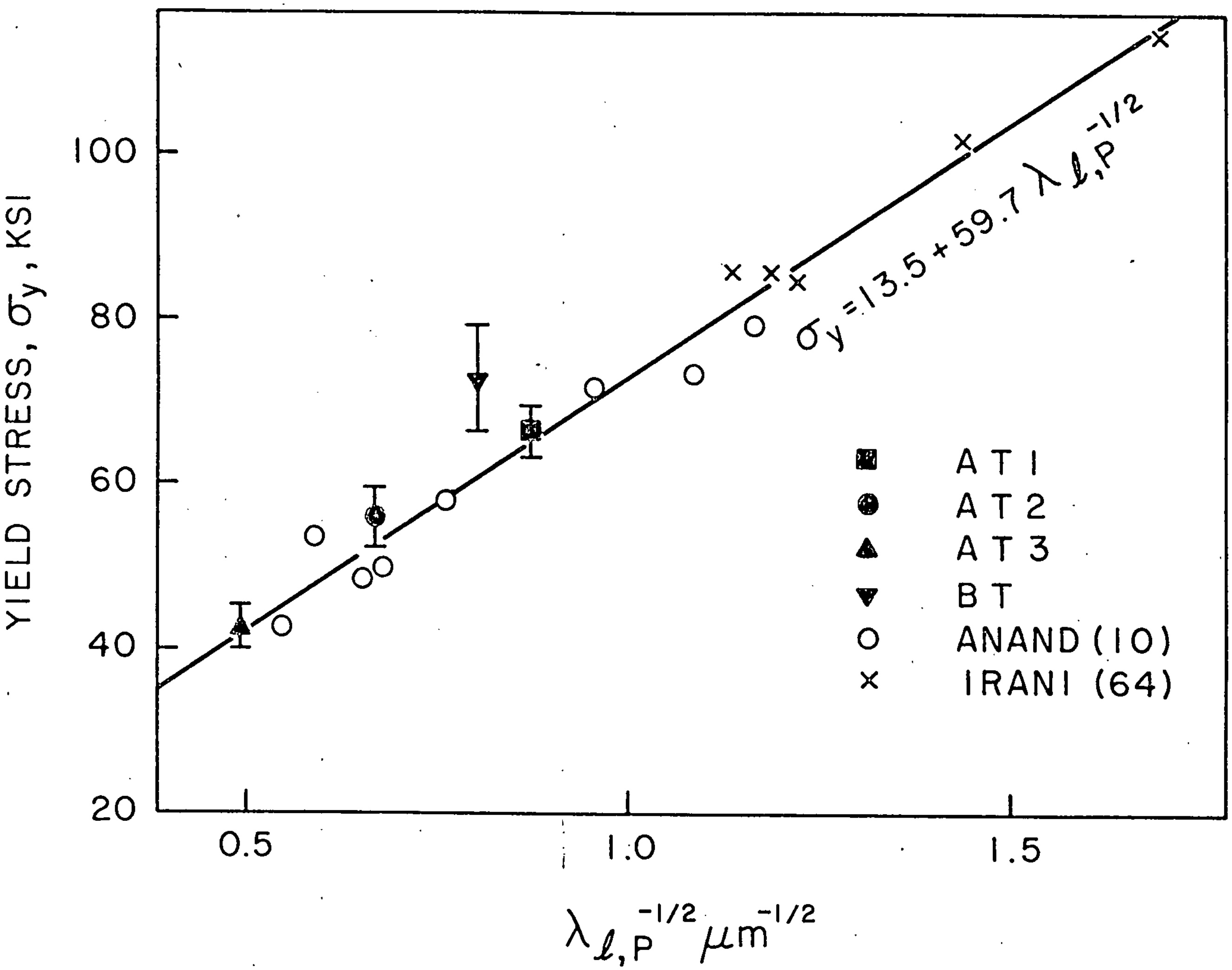
YIELD STRESS, σ_y, KSI
100
80
60
40
20
0.5
1.0
1.5
$\lambda_{\ell,P}^{-1/2}\ \mu m^{-1/2}$
$\sigma_y = 13.5 + 59.7\,\lambda_{\ell,P}^{-1/2}$
■ AT 1
● AT 2
▲ AT 3
▼ BT
○ ANAND (10)
× IRANI (64)

FIGURE 5.8

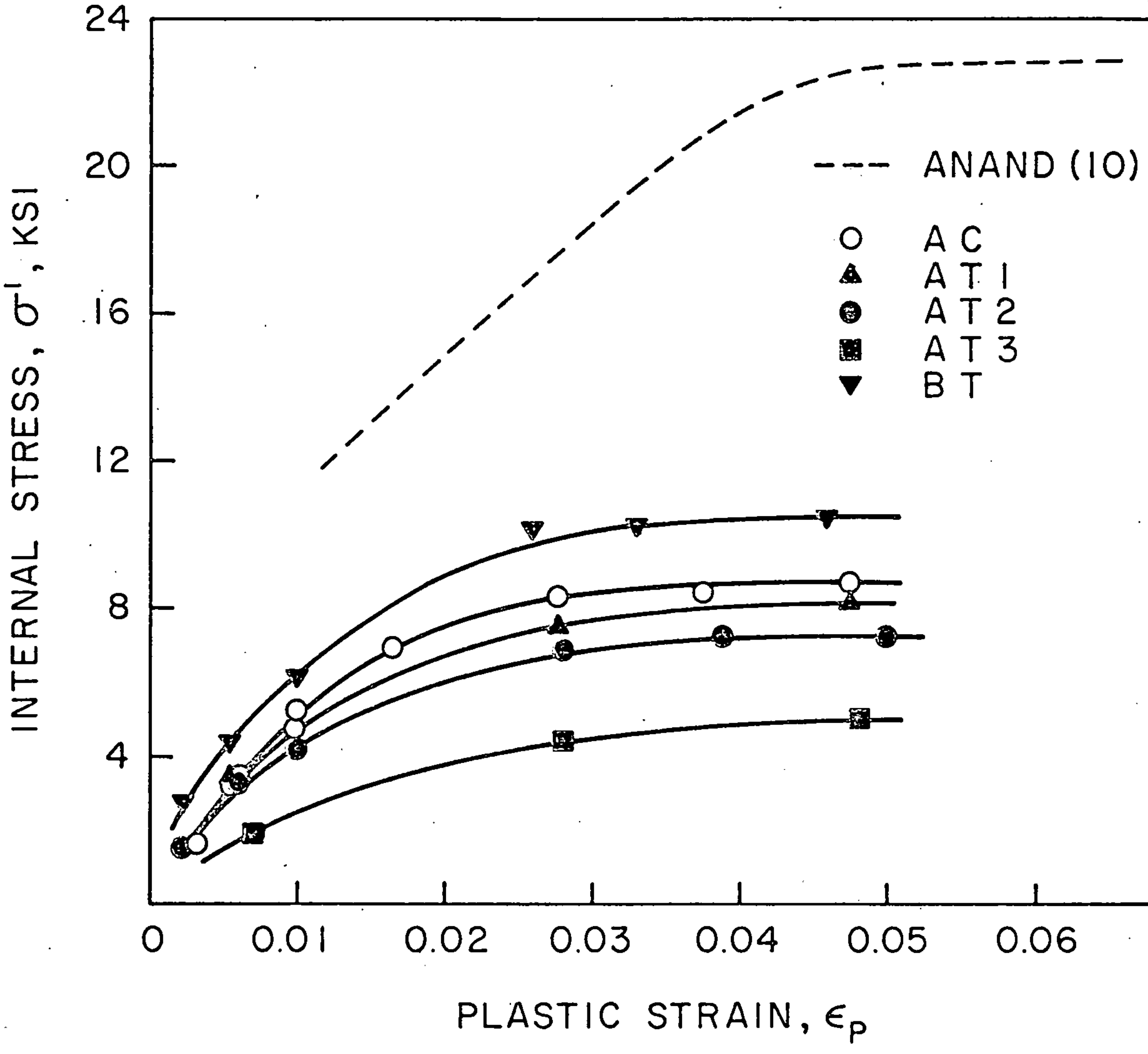
24
20
16
12
8
4
0
0.01
0.02
0.03
0.04
0.05
0.06
INTERNAL STRESS, σ^i, KSI
PLASTIC STRAIN, ϵ_p
--- ANAND (10)
○ A C
▲ A T 1
● A T 2
■ A T 3
▼ B T

FIGURE 5.9

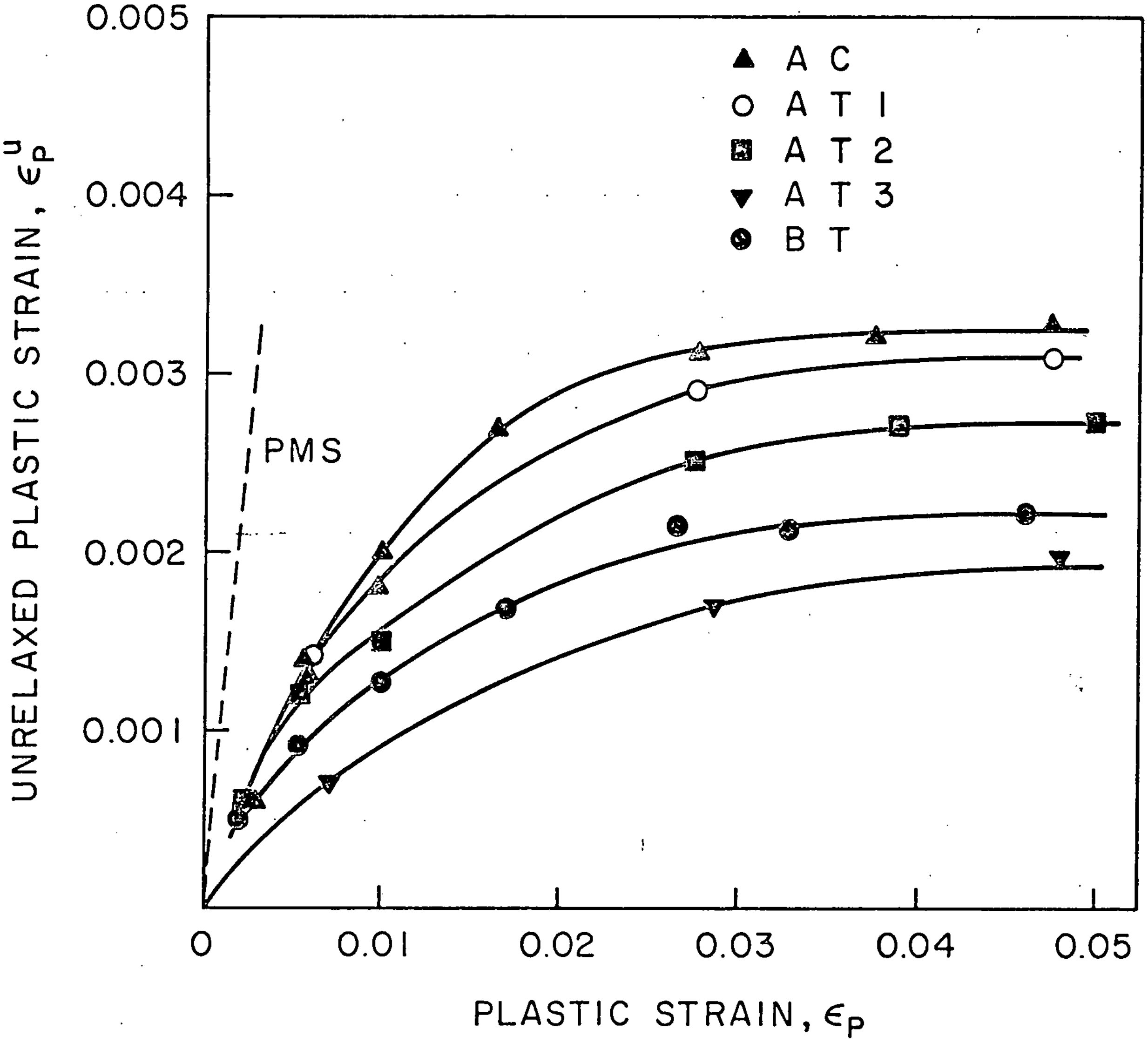
0.005
0.004
0.003
0.002
0.001
0
0.01
0.02
0.03
0.04
0.05
UNRELAXED PLASTIC STRAIN, ϵ_P^u
PLASTIC STRAIN, ϵ_P
PMS
▲ A C
○ A T 1
▣ A T 2
▼ A T 3
● B T

FIGURE 5.10

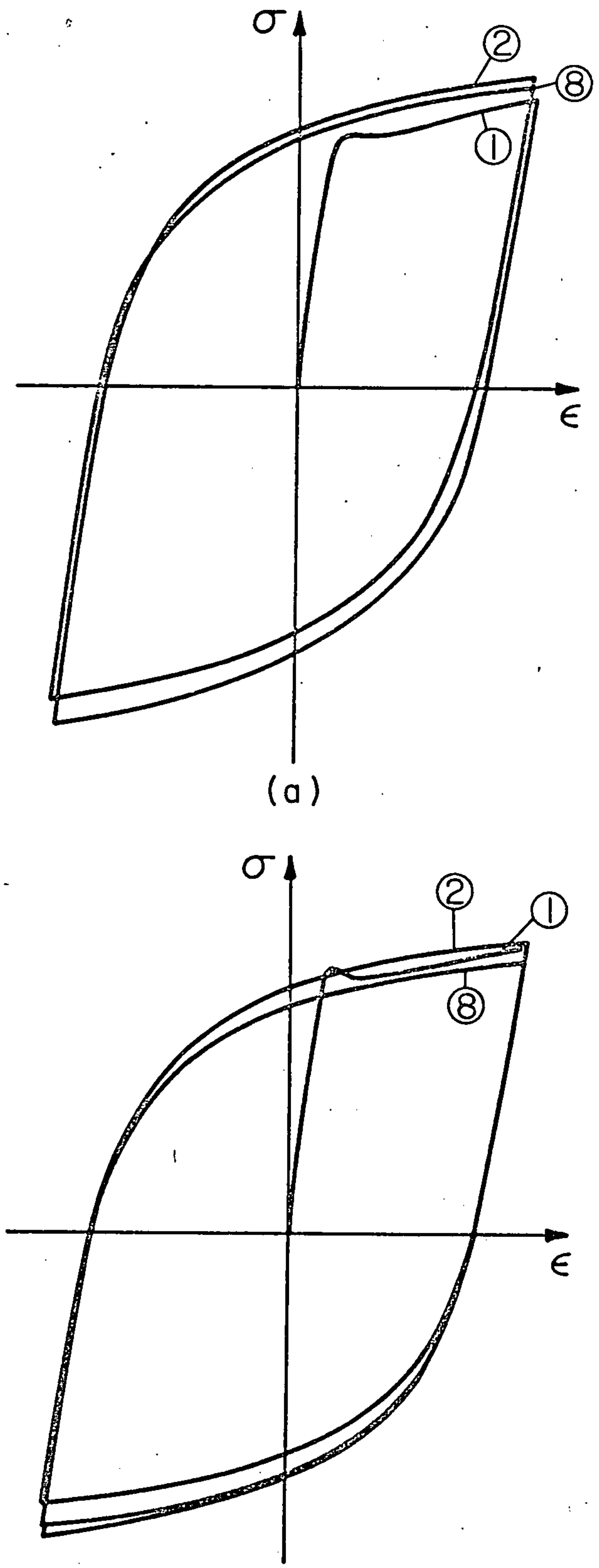

(a)

(b)

FIGURE 5.11

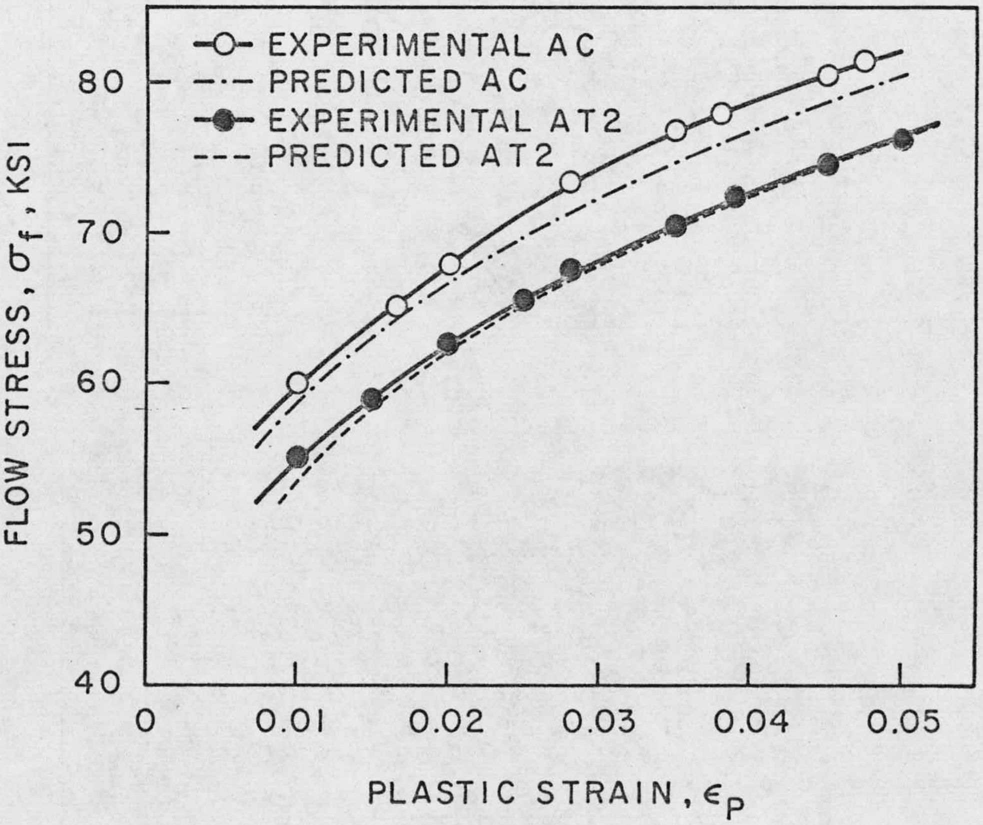
EXPERIMENTAL AC
PREDICTED AC
EXPERIMENTAL AT2
PREDICTED AT2
FLOW STRESS, σ_f, KSI
80
70
60
50
40
0
0.01
0.02
0.03
0.04
0.05
PLASTIC STRAIN, ϵ_P

FIGURE 5.12

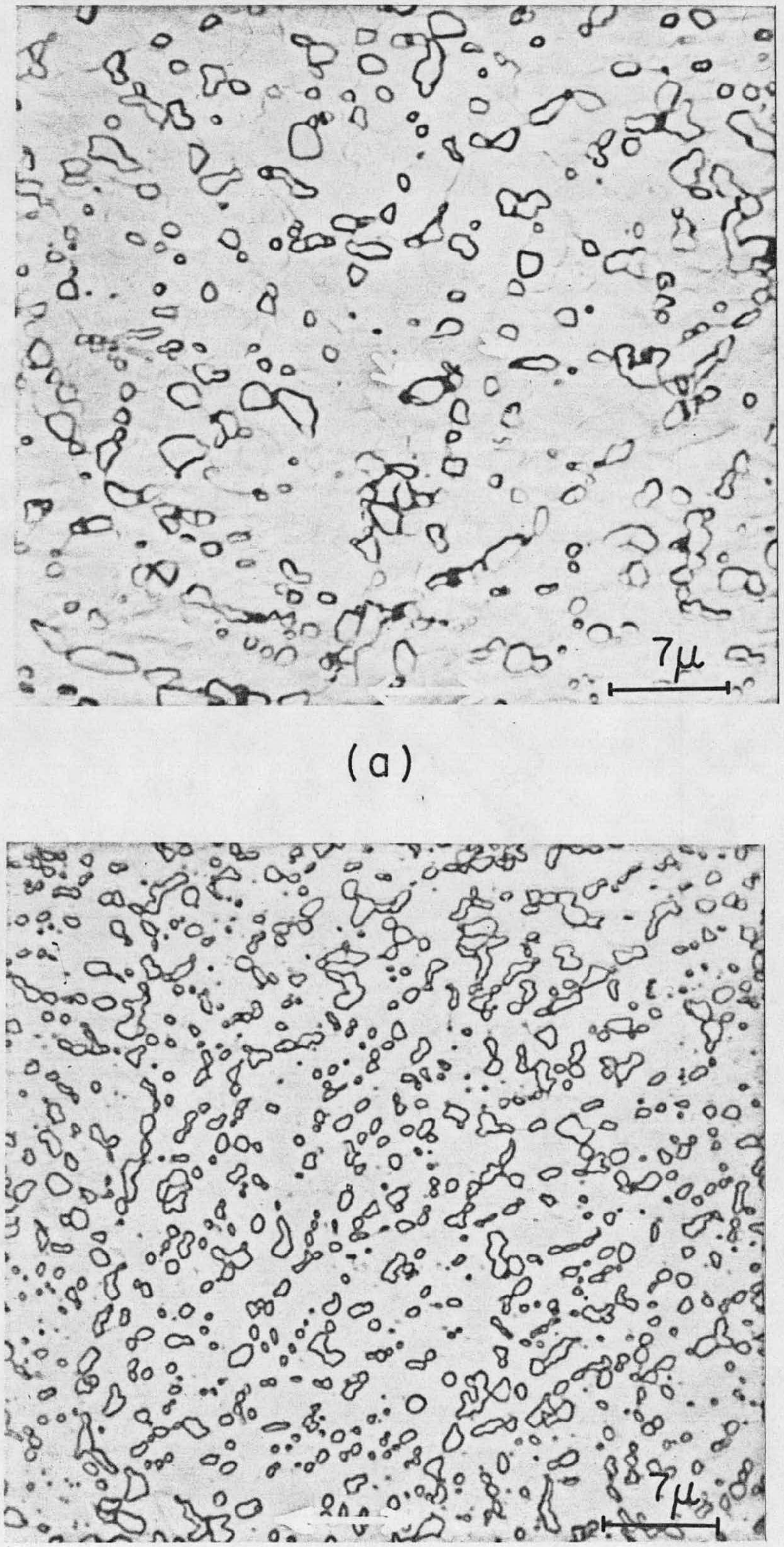

(a)

(b)

FIGURE 5.13